MINIMALLY-INVASIVE LENS-FREE COMPUTATIONAL MICROENDOSCOPY

by

Jaewook Shin

A dissertation submitted to The Johns Hopkins University
in conformity with the requirements for the degree of
Doctor of Philosophy

Baltimore, Maryland

October, 2019

Abstract

Ultra-miniaturized imaging tools are vital for numerous biomedical applications. Such minimally-invasive imagers allow for navigation into hard-to-reach regions and, for example, observation of deep brain activity in freely moving animals with minimal ancillary tissue damage. Conventional solutions employ distal microlenses. However, as lenses become smaller and thus less invasive they develop greater optical aberrations, requiring bulkier compound designs with restricted field-of-view. In addition, tools capable of 3-dimensional volumetric imaging require components that physically scan the focal plane, which ultimately increases the distal complexity, footprint, and weight. Simply put, minimally-invasive imaging systems have limited information capacity due to their given cross-sectional area.

This thesis explores minimally-invasive lens-free microendoscopy enabled by a successful integration of signal processing, optical hardware, and image reconstruction algorithms. Several computational microendoscopy architectures that simultaneously achieve miniaturization and high information content are presented. Leveraging the computational imaging techniques enables color-resolved imaging with wide field-of-view, and 3-dimensional volumetric reconstruction of an unknown scene using a single camera frame without

any actuated parts, further advancing the performance versus invasiveness of microendoscopy.

Thesis Committee

Primary Reader: Mark A. Foster

Secondary Reader: Trac D. Tran

Acknowledgments

I would like to thank my advisor Dr. Mark Foster for his support and patience throughout my graduate studies. I have truly learned a lot from his guidance, optimism, vast knowledge, and passion for science. I would also like to thank Dr. Trac Tran, Dr. Sang Chin, and Dr. Amy Foster for their support in our collaborative projects. This work would not have been possible if not for their contributions.

I would like to thank the following colleagues for their valuable discussions and input: Jasper Stroud, Bryan Bosworth, Milad Alemohammad, Dung Tran, Neil MacFarlane, Kangmei Li, Hongcheng Sun, and Michael Kossey.

Dedication

To my parents and my sister

Kwangyong Shin, Jungmin Park and Jaeyeon Shin

who have guided and supported me through my life.

Table of Contents

List of Figures

Chapter 1

Introduction

Optical endoscopes are widely used to image the interior of the human body, enabling disease diagnosis and surgical image guidance. In addition, fiber-optic micoendoscopes are becoming extremely valuable tools for structural and functional brain imaging of live animals. Such behavioral studies demand tools with high spatio-temporal resolution that can image over a large space to capture large-scale neural activity deep in the brain [1]–[10]. Many investigations are being made to develop minimally-invasive tools that enable functional mapping of the brain for degenerative disease studies or gain insight towards neuromorphic computing. However, conventional imaging architectures have limited information capacity due to the physical constraints of the optics and electronics. Every imaging system exhibits inherent trade-offs, such as that between spatial resolution and field-of-view. There is the trade-off between resolution and imaging speed, as conventional camera sensors read out each pixel information serially and thus achieve faster imaging speed at the cost of pixels. In addition, acquisition of higher-dimensional data such as a 3-dimensional volumetric scene or a hyperspectral image require

additional scanning mechanisms which ultimately sacrifice the imaging speed. Notably, microlenses that are ubiquitously used in minimally-invasive imaging applications exhibit tremendous optical distortions, including spherical and chromatic aberrations, and field-of-view limited to hundreds of μm.

This thesis explores several approaches to computational microendoscopy which aim to surpass these physical constraints using novel image reconstruction algorithms and paradigm shift in the optical hardware. The following introduction describes the background in optics and signal processing to understand this work. In addition, state-of-the-art imaging systems for minimally-invasive applications are described, including their respective shortcomings. Proceeding chapters present my work in ultra-thin microendoscopy enabled by computational imaging techniques. Specifically, these novel imaging probes employ a coded-aperture or a scattering medium at the distal end of an optical fiber to reconstruct an unknown scene using iterative optimization algorithms. Last chapter describes other computational optical imaging architectures that are in development for two-photon microscopy and ultra-fast imaging, followed by a few concluding remarks.

1.1   Ray Optics

Ray optics, also known as geometrical optics, is an approximation theory to describe the light propagation as straight lines or rays. Most of our daily experiences with light can be explained with ray optics, and it is an excellent approximation when the wavelength of light is small compared to the optical media that it interacts with. This technique is used to describe the location

and direction of light rays and thus useful to describe the image formation of lenses including their optical aberrations. In addition, it is used to determine the conditions under which light is *guided* in a given medium, such as in an optical fiber. Several ray optics principles that are most relevant to this thesis are explained.

1.1.1 Light Guides
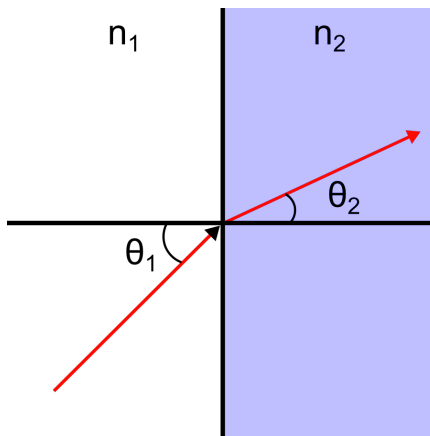
Figure 1.1: Illustration of Snell's Law.

An optical medium is characterized by a quantity $n \geq 1$ called the refractive index. The refractive index is $n = \frac{c_o}{c}$ where c_o and c are the speeds of light in free space and in the medium. Thus the optical path length in the medium is nd for some distance d. An incident light ray at the boundary between two media with refractive indices n_1 and n_2 are split in two: reflected ray and a refracted ray. The refracted ray obeys the Snell's law and is shown in Figure 1.1.

$$n_1 \sin \theta_1 = n_2 \sin \theta_2 \tag{1.1}$$

where θ_1 and θ_2 are the incident and refracted angles. Note that the proportion of the reflected and refracted light are not described in this postulate.

The incident light ray experiences total internal reflection when $\theta_2 = \frac{\pi}{2}$, known as the critical angle given as follows:

$$\theta_c = \sin^{-1}\left(\frac{n_2}{n_1}\right) \tag{1.2}$$

A suitable light guide mechanism is that of the total internal reflection at the boundary between two media with different refractive indices. As an example, Figure 1.2 shows an optical fiber in which light rays are guided by multiple total internal reflections.
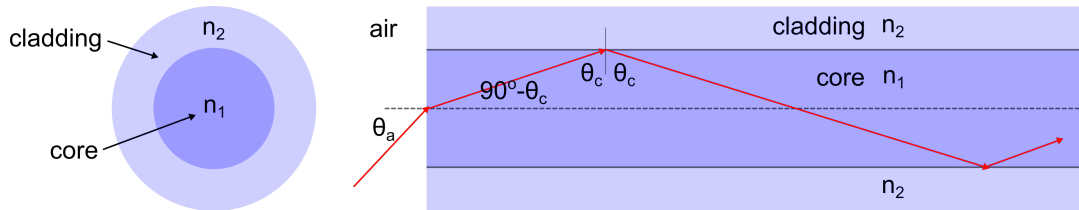
Figure 1.2: Optical fiber and its maximum acceptance angle.

The maximum acceptance angle of the optical fiber is given as follows:

$$\text{NA} = \sin\theta_a = \sqrt{n_1^2 - n_2^2} \tag{1.3}$$

where NA is known as the numerical aperture of the fiber and θ_a is the acceptance angle.

1.1.2 Image Formation

A spherical lens is a combination of two spherical boundaries, which are air-to-glass and glass-to-air. For simplicity we make the assumption that the lens is thin; the height at which the light ray enters is identical to the height at which the ray leaves. The image formation of a thin lens is then described as follows:

$$\frac{1}{f} = \frac{1}{d_o} + \frac{1}{d_i} \tag{1.4}$$

where f is the focal length of the lens, d_o is the distance between the object and the lens, and d_i is the distance between the lens and the image formed. The magnification factor of the image formed is $M = -\frac{d_i}{d_o}$, and the numerical aperture of the thin lens is approximated as $\text{NA} \approx \frac{D}{2f}$ where D is the entrance pupil of the lens. Figure 1.3 shows examples of image formation using a single lens and two lenses, known as a 4f system. Note that beyond ray optics, a 4f system is used in many optical-computing applications in addition to imaging. A lens has 2D Fourier Transform property; if an object is placed one focal length in front of a lens, then its Fourier transform will be formed at the other focal length behind the lens. As an example, a 4f system can be used to perform spatial filtering by placing an amplitude mask at the Fourier plane, optically filtering out the undesired 2D spatial frequencies.

1.1.3 Pinhole Camera

Pinhole camera is an excellent example of ray optics at work. It is the simplest lens-free camera that employs a tiny aperture (i.e. pinhole) close to an image

(A)

(B)
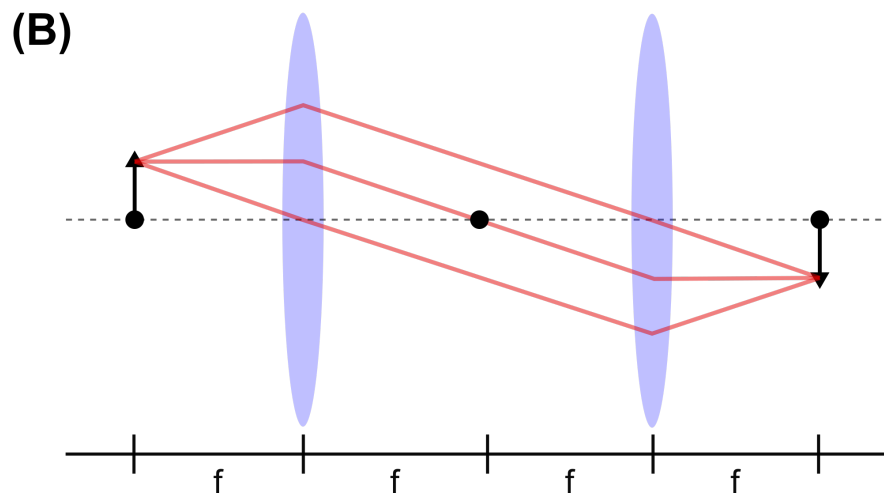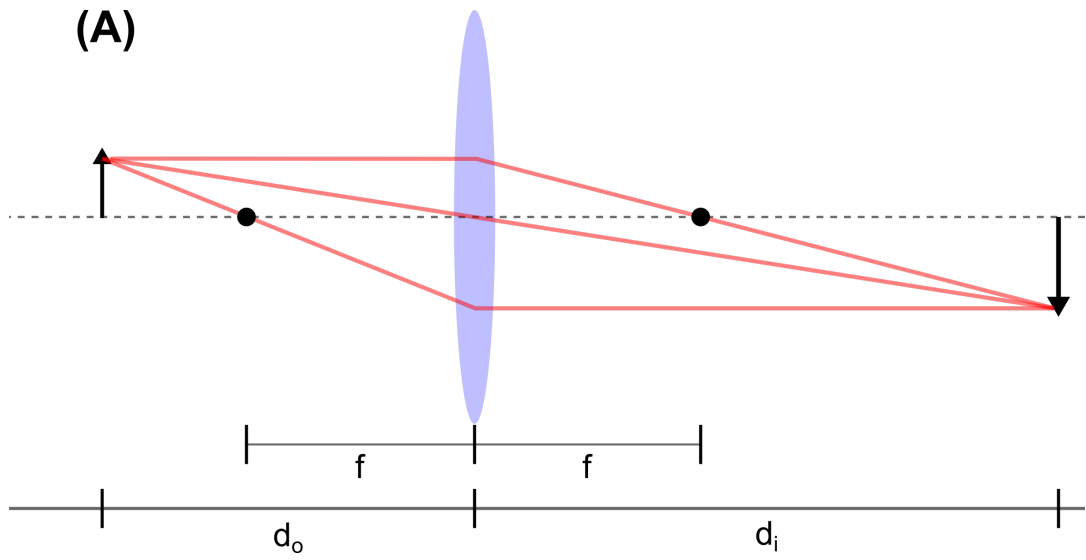
Figure 1.3: (A)(B) Image formation using a single lens and two lenses (4f system).
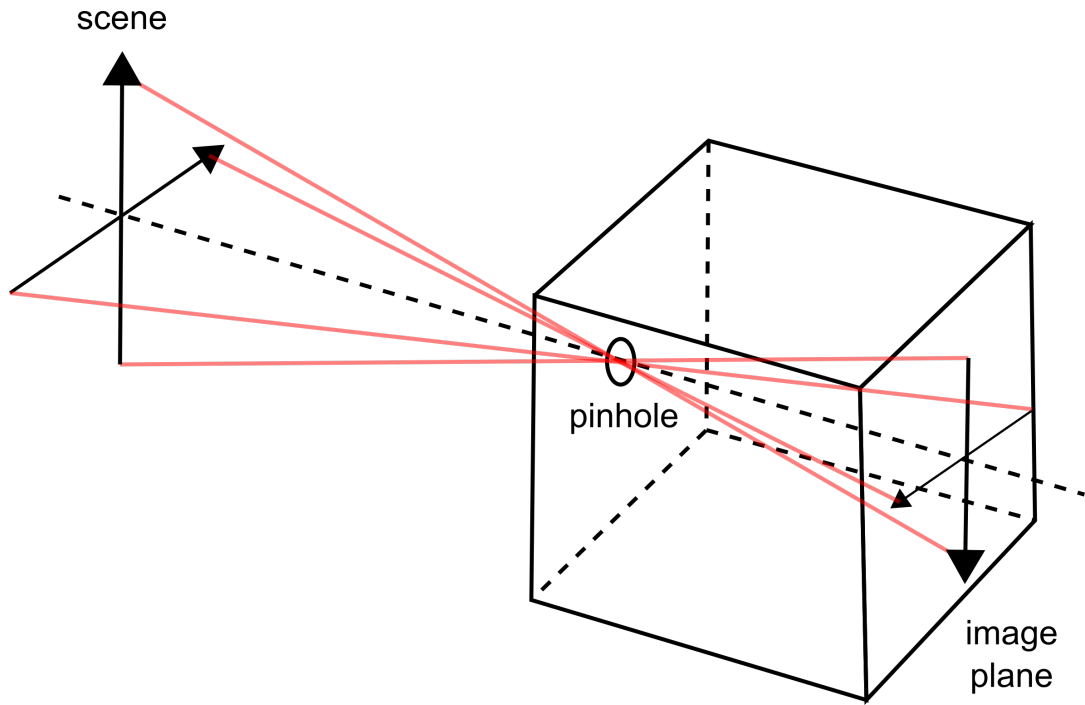
Figure 1.4: Illustration of a pinhole camera.

sensor. As shown in Figure 1.4, the working principle of a pinhole camera is that the tiny aperture rejects all light rays that do not contribute to the image formation. A pinhole camera only detects the light rays emitted from the object and thus in principle have an infinite depth of field. Notably, the resolution limit as a function of the pinhole diameter is expressed as follows:

$$f = \frac{s^2}{\lambda} \tag{1.5}$$

where f is the focal length, s is the pinhole radius, and λ is the wavelength of light. Here the focal length is $\frac{1}{f} = \frac{1}{d_o} + \frac{1}{d_i}$ where d_o is the distance between a scene and the pinhole, while d_i is the distance between the pinhole and the image plane. As shown in [11], the best resolution is achieved when

7

$f = \frac{s^2}{\lambda} = 1$. Here, the pinhole camera operates in the near-field regime in which the pinhole acts as a Fresnel zone plate and focuses the light slightly, generating the smallest possible spot on the observation plane.

Main reason why pinhole cameras, despite their compelling features including infinite depths of field and no spherical aberrations, are barely used is its extremely low light collection. A tiny pinhole readily forms a sharp image but simultaneously rejects majority of the light from the scene. However, what if we have an imaging system with an array of pinholes to increase the light throughput? Is it possible to deconvolve the image information from whatever mess we detect on the sensor? These questions will be answered in Chapter 2 which presents a computational microendoscope employing a coded-aperture (i.e. an array of randomly located pinholes).

1.2 Wave Optics

As the name suggests, the fundamental principle behind wave optics is that light propagates in waves, which is described by a second-order differential equation known as the wave equation. Specifically, wave optics describes optical phenomena that fall outside of ray optics, such as interference and diffraction effects. Again, this chapter describes a few wave optics postulates most relevant to this thesis.

1.2.1 Wave Equation

Let $a(\mathbf{r}), \phi(\mathbf{r}), w$ represent the amplitude, phase, and angular frequency as a function of position $\mathbf{r} = (x, y, z)$. A real wave function $u(\mathbf{r}, t)$ can be described

in terms of the following complex function:

$$U(\mathbf{r}, t) = a(\mathbf{r}) \, e^{j\phi(\mathbf{r})} \, e^{jwt} \tag{1.6}$$

so that

$$u(\mathbf{r}, t) = \text{Re}\left\{ U(\mathbf{r}, t) \right\} = \frac{1}{2}\left(U(\mathbf{r}, t) + \overline{U}(\mathbf{r}, t) \right) \tag{1.7}$$

where $\overline{U}$ is the complex conjugate. The complex wave function $U(\mathbf{r}, t)$ must satisfy the following second-order differential equation:

$$\nabla^2 U - \frac{1}{c^2}\frac{\partial^2 U}{\partial t^2} = 0 \tag{1.8}$$

where c is the speed of light in a medium of refractive index n and $\nabla^2 = \frac{\partial^2}{\partial x^2} + \frac{\partial^2}{\partial y^2} + \frac{\partial^2}{\partial z^2}$. In addition, a wave can be written as a linear combination of other solutions to the wave equation, e.g., $U(\mathbf{r}, t) = U_1(\mathbf{r}, t) + U_2(\mathbf{r}, t)$.

1.2.2 Wave Interference

The optical intensity $I(\mathbf{r})$ of a monochromatic light (single wavelength and frequency) is defined as the optical power per unit area (Watts/cm^2), and written as follows:

$$I(\mathbf{r}) = |U(\mathbf{r})|^2 \tag{1.9}$$

where $U(\mathbf{r}, t) = a(\mathbf{r}) \, e^{j\phi(\mathbf{r})} \, e^{jwt} = U(\mathbf{r}) \, e^{jwt}$ and $U(\mathbf{r})$ is the complex amplitude. Consequently, intensity of the interference between two monochromatic light with complex amplitudes $U_1(\mathbf{r})$ and $U_2(\mathbf{r})$ is derived as follows:

$$U(\mathbf{r}) = U_1(\mathbf{r}) + U_2(\mathbf{r}) \tag{1.10}$$

9

$$I = |U|^2 = |U_1|^2 + |U_2|^2 + \overline{U_1}U_2 + U_1\overline{U_2} \qquad (1.11)$$

where $U_1 = \sqrt{I_1}\, e^{j\phi_1}$ and $U_2 = \sqrt{I_2}\, e^{j\phi_2}$. Thus,

$$I = I_1 + I_2 + 2\sqrt{I_1 I_2}\, \cos(\phi_2 - \phi_1) \qquad (1.12)$$

This is known as the interference equation, and it can be readily seen that the intensity of the sum of two waves has an additional cosine term that is phase-dependent. The dependence of I on ϕ allows the measurement of phase differences by detecting the corresponding light intensity, and reversibly, generation of a light intensity by engineering the appropriate phase. The interference intensities from a coherent light and utilizing it for imaging with high information content will be further explored in Chapter 3 and 4.

1.3 Space-Bandwidth Product

A common metric used to characterize the information capacity of an optical system is the space-bandwidth product (SBP) [12]. Specifically, SBP is the number of effective pixels required to capture the full information transmitted by an optical imaging system, and is written as follows:

$$\text{SBP} = \frac{\text{field-of-view}}{(\text{Nyquist resolution})^2} \qquad (1.13)$$

In other words, this is the field-of-view area divided by the pixel size required to achieve Nyquist sampling. As an example, an imaging system with a 1-mm^2 field-of-view and 10-μm spatial resolution has a SBP $= \frac{1 \text{ mm}^2}{(5\ \mu\text{m})^2} = 40,000$. This metric will be used throughout this thesis to characterize the performance

of microendoscopy systems.

1.4   Compressive Sensing and Imaging

Compressive sensing (CS) is a sampling paradigm developed in 2006 that leverages the natural sparsity of real signals. The fundamental principle behind CS is that a signal of interest can be sampled and reconstructed with far fewer measurements than that dictated by the Nyquist sampling criterion if it can be sparsely represented in some mathematical basis [13]–[16]. Contrary to conventional imaging architectures that acquire each pixel information sequentially, i.e. raster-scanning, compressive imaging systems directly measure the inner products between a scene of interest and known patterns. Consequently, these compressed measurements and the projection patterns are used to solve a sparse optimization problem to reconstruct the scene with high fidelity.

This novel sampling approach can be especially useful in imaging or sensing architectures where signal measurements are limited under various conditions resulting in strict limits to the amount of acquired image information. Specifically, an ultra-miniaturized imager such as a microendoscope that has a limited number of measurements for a given cross-sectional area can benefit tremendously with this sampling approach.

1.4.1   Data Compression

Decades of research in data compression technology have ushered today's digital world. Efficient storage and transmission of audio, image, and video
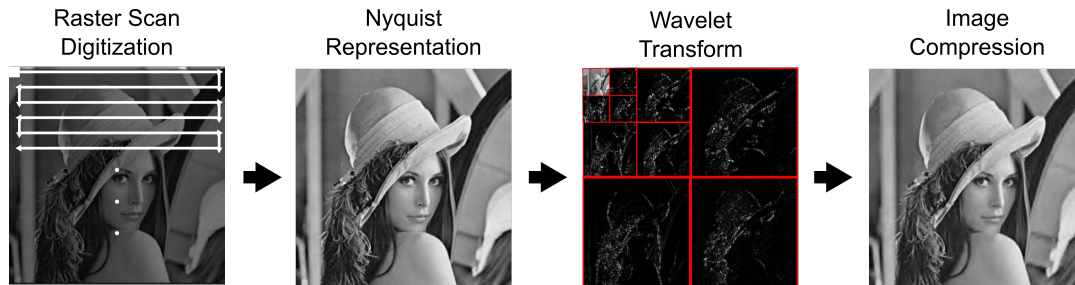
Figure 1.5: Flowchart of a conventional image compression. Lena image is first digitized at the Nyquist sampling rate. The raw data is then compressed using a 3-level 4th-order Daubechies basis where only the highest 10% of the coefficients are kept and used for the image reconstruction.

signals has enabled popular streaming media as well as user-generated content. The key principle behind data compression is to sparsely represent the data using some mathematical basis, so that majority of its transform coefficients can be discarded without perceptual loss [13], [14]. In a conventional image compression architecture, the raw image of a scene is first sampled and digitized using N number of pixel sensors on a CCD or CMOS imaging chip. This raw data is then transformed to a sparse domain using known basis functions, such as discrete cosine or multi-level wavelet. These basis functions are capable of representing an image with a few significant coefficients (i.e. weights applied to each basis function), so that the majority are close to zero and thus can be thresholded and discarded. As an example, Figure 1.5 demonstrates such image compression using a 3-level 4th-order Daubechies basis; Lena image is sparsity-transformed where only the highest 10% coefficients are kept while the rest are hard-thresholded. It can be seen that the image reconstruction using only 10% of the significant coefficients still maintains the perceptual quality. Decades of research in sparse representation and signal processing have laid the foundation in compressive sensing, as it advocates a

more efficient sampling by implementing the data compression directly at the signal acquisition stage.

1.4.2 Mathematical Model
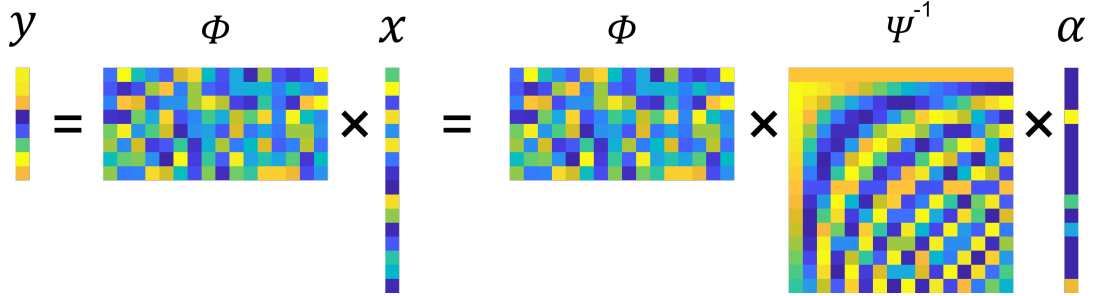
Figure 1.6: Visualization of the matrix multiplications in compressive sensing. The objective is to recover the signal of interest x from an observation vector y, measurement functions (sensing matrix) Φ, and a known sparsifying transform Ψ. As an example, Ψ is shown as the discrete cosine transform which sparsity-transforms x to α with 4 non-zero elements.

In essence, compressive sensing finds a solution to underdetermined linear systems and is written as the following matrix multiplication. Let M and N represent the number of observations (compressed measurements) and the Nyquist dimension of an object image. The observation vector $y \in \Re^{M \times 1}$ can be expressed as the following:

$$y = \Phi x = \begin{bmatrix} \phi_1 x \\ \phi_2 x \\ \vdots \\ \phi_M x \end{bmatrix} \tag{1.14}$$

where ϕ_1, ϕ_2, ..., $\phi_M \in \Re^{1 \times N}$ are vectorized measurement functions, and $x \in \Re^{N \times 1}$ is the vectorized object image. The sensing matrix Φ consists of M measurement functions vertically concatenated. The objective is to solve

for the signal of interest x from observations y and measurement functions Φ. In Nyquist sampling, $M = N$ and the sensing matrix is an N by N identity matrix for a raster scan, or a Nyquist set of basis functions, such as the Hadamard basis. In compressive sensing, $M < N$ and thus enforces a sparsity regularization to find the correct solution of x from infinitely many possible solutions. As mentioned in previous section, there are mathematical basis or dictionary in which x is sparse with very few significant coefficients. This is formulated as $\alpha = \Psi x$ where $\Psi \in \Re^{N \times N}$ is the sparsifying transform, and $\alpha \in \Re^{N \times 1}$ is a K-sparse vector with K non-zero elements. Consequently, the sensing problem is written as $y = A\alpha$ where $A = \Phi\Psi^{-1}$, as shown in Figure 1.6. In order to solve such ill-posed problem the sensing matrix must meet the Restricted Isometry Property (RIP) [16]. The sensing matrix A satisfies the RIP of K-sparse signal if there exists a bound $0 < \delta_K < 1$ such that

$$(1 - \delta_K)||\alpha||_2^2 \leq ||A\alpha||_2^2 \leq (1 + \delta_K)||\alpha||_2^2 \tag{1.15}$$

holds for all $\alpha \in \sum_K$. The sensing matrix A meets the RIP requirement if it has a minimum coherence, which is defined as the largest absolute inner product between any of its two normalized columns. Typically, a sensing matrix of i.i.d random entries is employed as it satisfies the RIP and leads to the recovery of x with high probability by solving the following ℓ_1-minimization problem.

$$\min_{\alpha} ||\alpha||_1 \text{ s.t. } ||y - \Phi\Psi^{-1}\alpha||_2 \leq \sigma. \tag{1.16}$$

where σ is some noise boundary. Intuitively, such random sensing matrix

works with a high probability of success because the random projections are maximally uncorrelated with the common mathematical bases as well as with the unknown signal of interest. In accordance with compressive sensing theory, the minimum number of observations to accurately reconstruct x is defined as $K \log\left(\frac{N}{K}\right) \leq M$ where K is the signal sparsity.

1.4.3 Hardware Implementation
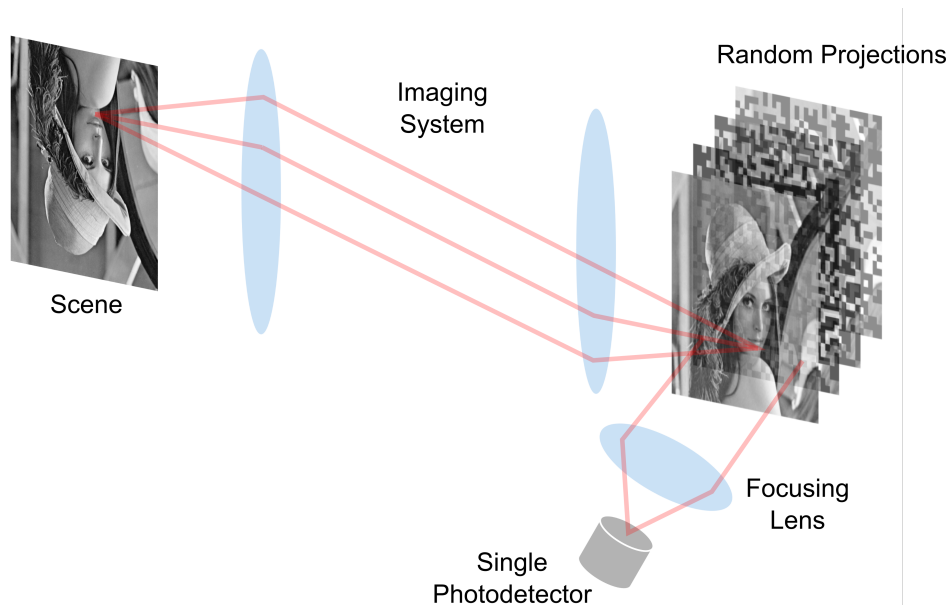
Figure 1.7: Illustration of a compressive imaging architecture: single-pixel camera. A spatial light modulator is employed to sequentially mask or illuminate the scene with pseudorandom patterns. A lens is used to focus the reflected light to a single photodetector, which measures the optically-computed inner products between the pseudorandom projections and the scene.

A conventional imaging system digitizes the raw data of an object image via point-scan, which acquires each pixel information sequentially. The raw data undergoes an image compression routine where it is mapped to a sparse mathematical domain. Although an encoder can represent the object

image using very few significant coefficients, a lot of the hardware resources used to sample the raw image are effectively wasted. Compressive sensing hardware implements the compression directly at the signal acquisition stage. Notably, in CS imaging architectures, pseudorandom patterns are extensively used to sample a signal of interest, as they are highly uncorrelated with the mathematical bases in which natural images have sparse representation [13]–[16]. The inner product between these known patterns and the object are the compressed measurements used to reconstruct the object by solving a sparse optimization problem, such as minimizing the ℓ_1-norm of the object in its sparse form. Assuming the sampling patterns are sufficiently random to satisfy the RIP, one can reconstruct the object image using a highly sub-Nyquist number of measurements, where $M \ll N$. For optical implementation of CS imaging, a spatial light modulator (SLM) is commonly employed to either structure the incident light to generate pseudorandom illumination patterns or collection masks [17]–[20]. Such architectures are known as a single-pixel camera, since the inner products between the pseudorandom patterns and an object of interest are collected by a single-pixel photodetector instead of a pixel array in a CCD or CMOS imaging chip. The inner products are optically-computed as the light reflected or scattered from the scene is focused to a single photodetector using a focusing lens. Since the advent of the first single-pixel camera, much research has been done to develop more efficient and robust compressive sensing hardware. An interesting and recent development is the lensless camera based on coded-aperture imaging [21]–[24]. This architecture is quite relevant and will be discussed further in chapter 2. In short, the working principle is to place a single spatial mask

16

near the front of a bare sensor, followed by characterization of light propagation, i.e. point-spread-function, through the mask and onto the sensor. A sparsity-minimization algorithm is employed to reconstruct the scene using a single snapshot of the scene's coded-aperture response. Essentially, the lensless camera spatially-multiplexes the compressed measurements as each pixel measures the pseudorandom linear combination of light emitted from the scene. Contrary to single-pixel cameras that scan through the random projections via an SLM and acquire each measurement sequentially, the lensless camera acquires the measurements in a single shot, making this architecture suitable for high-speed, real-time imaging applications.
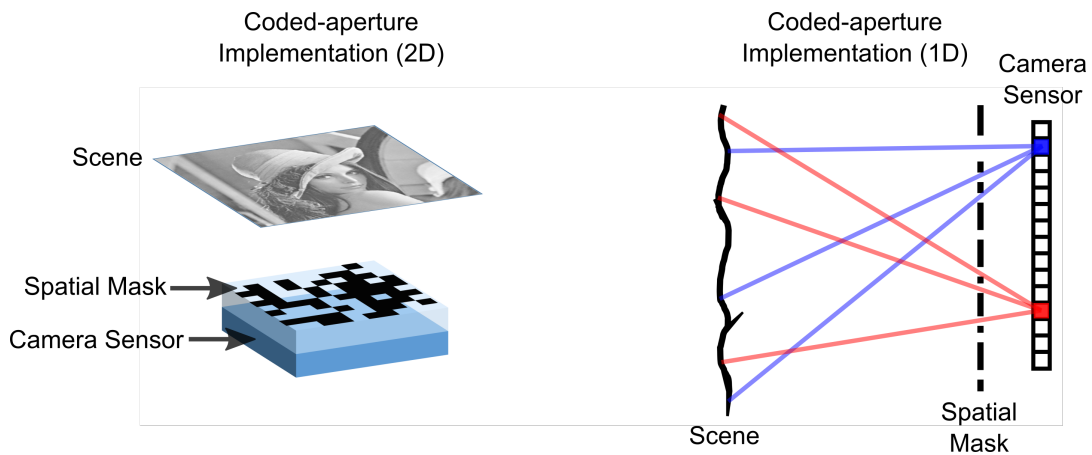
Figure 1.8: Schematic of a coded-aperture-based compressive imaging architecture. Contrary to the single-pixel camera, this lensless camera only requires a single pseudorandom mask which is integrated near a bare sensor, where each pixel measures the linear combination of light emitted from the scene. From the 1-dimensional illustration it can be readily seen that each sensor measures the light modulated by different regions of the coded-aperture, which spatially-multiplexes the compressed measurements.

1.5 Conventional Microendoscopy

Many investigations have been made in the field of microendoscopy to reduce the invasiveness of *in-vivo* imaging, while improving the imaging resolution, field-of-view (FOV), and 3-dimensional data acquisition. One current approach is to acquire each image pixel of a scene by distal scanning of a single-core fiber or proximal scanning using a multicore fiber. Here, distal end refers to the end of the optical fiber farthest from the source of illumination while proximal end is the other end of the optical fiber. Such microendoscope designs, shown in Figure 1.8, employ a mechanical scanner and microlenses, and recovers images with high spatial resolution but with a field-of-view limited by the deflection angle of the scanner.

Another approach is widefield illumination and detection using a multicore fiber or a fiber bundle, where fiber cores transmit the image pixels of a scene, as shown in Figure 1.9. In this case, widefield imaging is accompanied by a degradation in image quality due to the cross talk between fiber cores and pixelation artifacts. Furthermore, reducing the number of fiber cores improves miniaturization but reduces the field-of-view with the aforementioned effects becoming more pronounced. Alternatively, hand-held microscopes based on widefield illumination and collection using microlenses have been recently demonstrated for brain imaging of freely moving mice [5]–[8]. Regardless of the different approaches, the distal lenses that most approaches employ impose an inherent trade-off between miniaturization of the imaging probes and their imaging performance [5]–[8], [25]–[28]. The physical limit to miniaturization is a particular problem for brain imaging as probe implantation inevitably

18

(A) Distal Scanning Endoscope

Single Optical Fiber

Microlenses

Scene

(B) Proximal Scanning Endoscope

Multicore Fiber

Microlenses

Scene

(C) Miniaturized Microscope

Digital Data

Camera Sensor

Integrated Microscope

Microlens

Scene

(D) Widefield Illumination

Lens

Transmitted Image

Multicore Fiber

Microlens

Scene
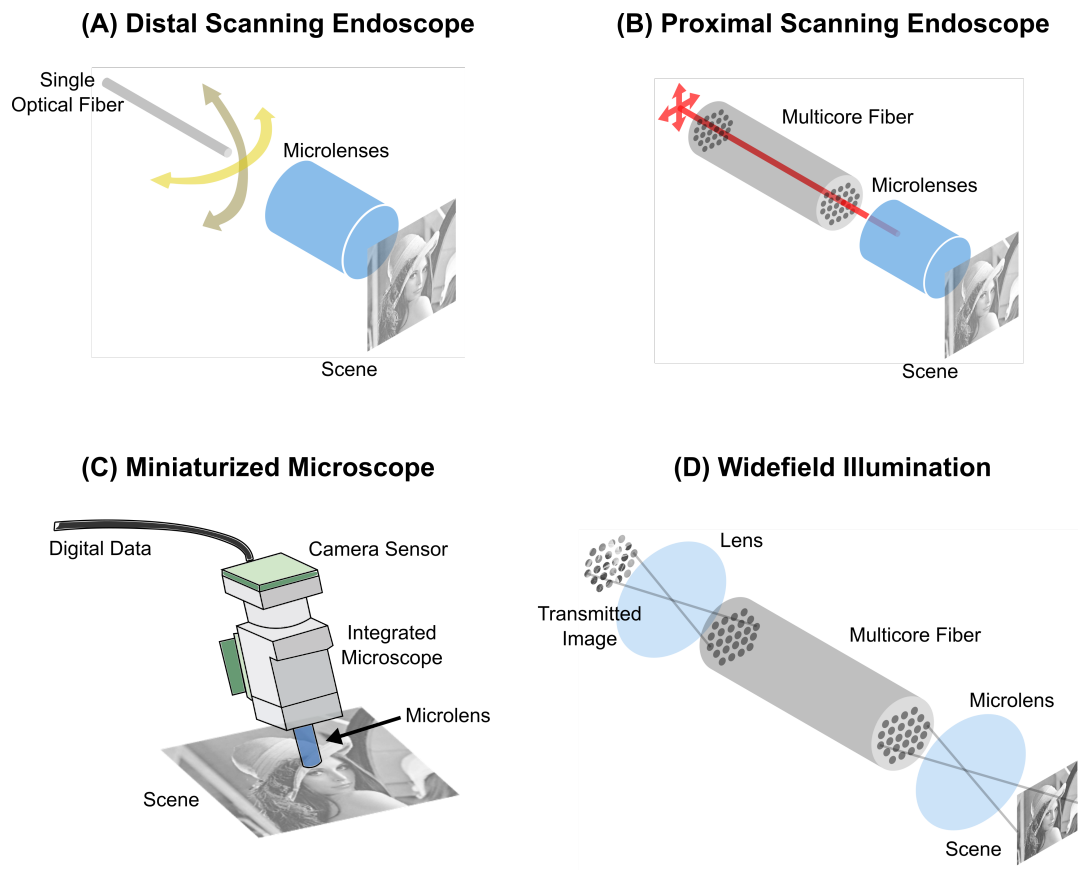
Figure 1.9: Conceptual illustration of conventional microendoscopy designs.

damages the intricate neural circuitry that such studies aim to understand [9], [10]. Figure 1.10 shows the relative dimensions between a mouse brain with 10s of mm in width, and a typical microlens that has a diameter of several mm. Most importantly, an animal brain is a 3-dimensional structure. For these microendoscopes to acquire 3-dimensional space they require components that physically vary the focal or imaging plane, such as a linear actuator or an electrically tunable lens. The increased distal footprint and weight of the probes makes brain mounting of freely moving animals more challenging [29]–[32].

Microlens (Ø 0.5~2mm)

Mouse Brain (width ~10mm)
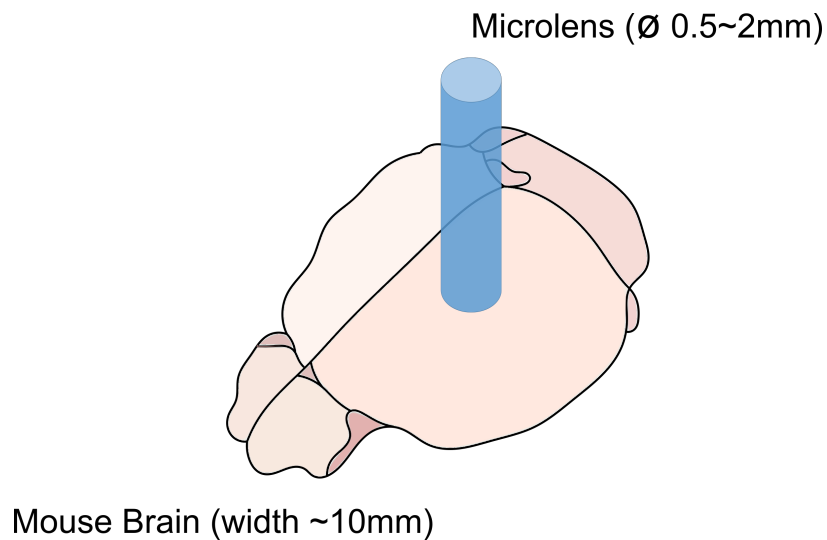
Figure 1.10: Illustration demonstrating the relative dimensions of a mouse brain and a typical microlens.

1.6 Lens-free Microendoscopy

Recently, many investigations have been made to develop a lens-free microendoscope. The main principle behind these lensless approaches is to precisely
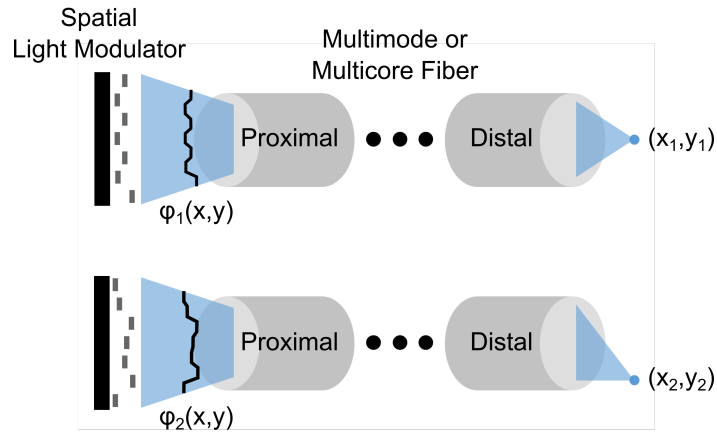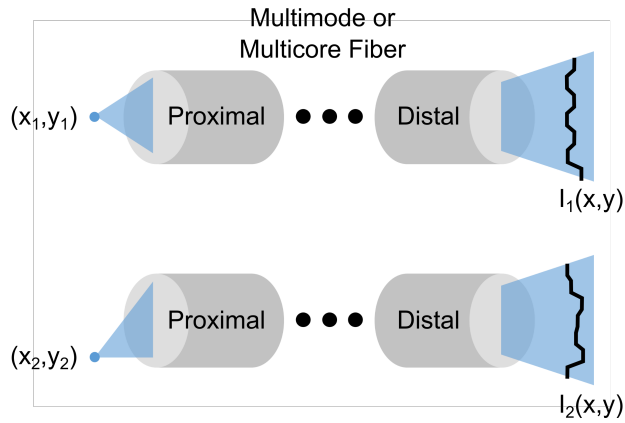
Figure 1.11: Concept of lensless microendoscope using a multimode or multicore fiber. **(A)** shows point scanning approach where a spatial light modulator generates the correct phase profile at the proximal end to generate a focused point at the distal end. **(B)** shows another imaging approach where a point source at the proximal end generates a complex speckle pattern at the distal end for structured illumination imaging. These lensless approaches are sensitive to bending of the fiber as they rely on the phase of guided light in each fiber core or spatial modes.

control the wavefront of a *coherent* light that couples into an ultra-thin waveguide, such as a multimode or multicore fiber. While these waveguides are extremely tiny ($\varnothing < 500\mu$m), they have complex light transmission characteristics due to the phase delays between different spatial modes or fiber cores. Thus, lensless imaging is enabled by fully characterizing the multi-modal light propagation through the fiber, and appropriately modulating the input phase. In essence, this is a holographic imaging method where the precise control of the phase at the proximal end can either generate a focus point at the distal end for a raster scan, or a series of structured illumination patterns that are post-processed to reconstruct a scene [33]–[38]. Unfortunately, the critical shortcoming of this approach is the extreme sensitivity to bending of the fiber and thus the inability to study freely-behaving animals. Fiber bending physically changes the optical path length (phase delays) between different modes or cores, which nullifies the transmission characterization. Several approaches have been suggested to address this issue but show drawbacks such as restricted field-of-view, inability to resolve color, reduced imaging contrast, or requiring an active calibration and feedback mechanism [38]–[41]. Importantly, the information content (i.e. space-bandwidth product) of these imagers are still limited by the total number of fiber cores or spatial modes.

Following chapters describe my work that demonstrates several approaches to ultra-thin lens-free microendoscopy enabled by computational imaging techniques and novel optical hardware. These imaging architectures are not only insensitive to bending of the imaging probe, but also capable of increasing the information content such as 3-dimensional volumetric reconstruction

using a single snapshot or image recovery with high-resolution and wide field-of-view.

Chapter 2

Computational Microendoscopy Using a Coded-Aperture

In this chapter, we combine coded-aperture imaging with a multicore fiber to create a distal lens-free microendoscope system that simultaneously achieves miniaturization and wide field-of-view. Figure 2.1 **(A)** shows simplified illustration of conventional lens-based imaging with a multicore fiber via widefield illumination and detection. Figure 2.1 **(B)** shows simplified illustration of the distal lensless imaging approach using a multicore fiber and a coded-aperture. In essence, distal lenses are replaced with a simple pseudorandom binary spatial mask (i.e. coded-aperture), which modulates the intensity of light propagating from the scene to the fiber face. Unlike the widefield illumination and collection approach, each fiber core serves as a single measurement instead of an image pixel as the cores measure a pseudorandom linear combination of light emitted from various points within the scene, enabling image reconstruction without pixelation artifacts.

Prior to imaging, we first characterize the light propagation through the coded-aperture and multicore fiber. For calibration, an *incoherent* light and a

A Conventional Lens-based Microendoscope
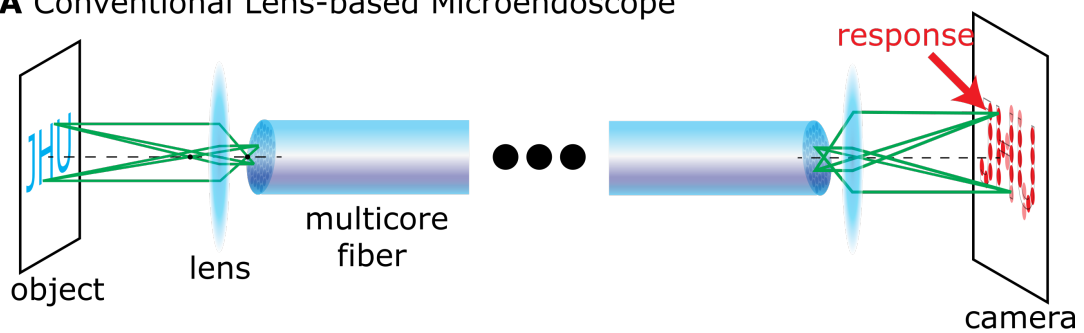
B Lensless Microendoscope using Coded Aperture
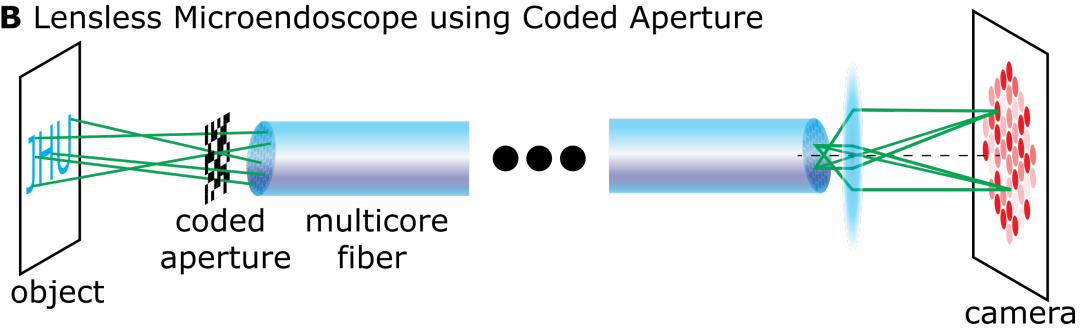
Figure 2.1: Minimally-invasive imaging using a multicore fiber and coded-aperture. **(A)** Simplified illustration of widefield illumination imaging using a multicore fiber and a lens. **(B)** Our distal lensless imaging approach using a coded-aperture.

digital micromirror device are used to project and scan a point source across the microscopic sample plane. The design of the calibration projector is described in below section. The light transmitted through the coded-aperture and multicore fiber is imaged at the proximal end of the multicore fiber onto a CCD camera, which captures the corresponding system response of each point source. For imaging, an object is placed in the sample plane, an incoherent light illuminates the sample plane, and a single snapshot of the object's system response is captured using the camera at the proximal end of the fiber. An image of the scene is then reconstructed using the calibrated system response of individual point sources, the single frame of the object's system response, and an ℓ_1-minimization image reconstruction algorithm. In comparison to previously demonstrated lensless approaches [33]–[38], the proposed lensless imager is insensitive to bending of the fiber as the operation relies on the faithful transmission of intensity patterns, not phase, of the system response of the point sources.

2.1 Mathematical Model

The above processes can be written mathematically as the following. Let M and N represent the number of fiber cores in the multicore fiber and number of pixels in the computational reconstruction, respectively. The imaging problem is then

$$y = Ax = \begin{bmatrix} A_1 x & A_2 x & \dots & A_N x \end{bmatrix} \tag{2.1}$$

where A_1, A_2, ..., $A_N \in \Re^{M \times 1}$ are the vectorized system responses from a spatially-varying point source, $y \in \Re^{M \times 1}$ is an object's system response, and $x \in \Re^{N \times 1}$ is the image of the object to be recovered. To reconstruct the image of the object from the object's system response, we utilize ℓ_1-minimization coupled with discrete cosine transform basis at the level of blocks of pixels called patches: any selected local patch should be sparse. Out of all candidate images that are consistent with the system response, the iterative optimization algorithm seeks out the most sparse set of overlapped patches. In accordance with compressive sensing theory, the minimum number of measurements, i.e. fiber cores, to accurately reconstruction x is defined as $K \log \left(\frac{N}{K} \right) \leq M$ where K is the number of non-zero elements in x and the calibration matrix satisfies the Restricted Isometry Property [16].

2.2 Reconstruction Algorithm
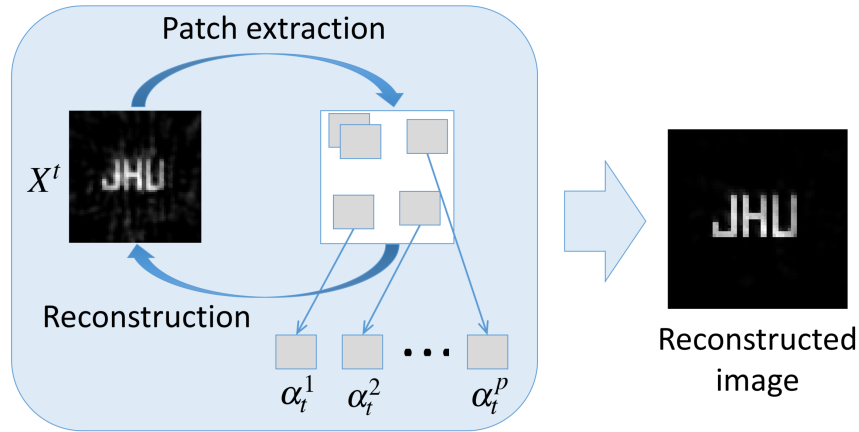
Figure 2.2: Illustration describing a patch-based iterative optimization algorithm, which iterates from global reconstruction of the image and sparsity regularization at the level of local patches. X^t and α_t^P represent the image estimate and DCT coefficients of overlapping patches at iteration t.

To reconstruct the image of the object from the object's system response, we utilize a reconstruction framework focusing on the local image structures. A popular model to quantify local image information is sparsity in an appropriate domain. Given a patch or block of pixels z extracted at a random location from the image of the object, its coefficients α under some sparsifying transform $\widetilde{\Psi}(\cdot)$ defined by

$$\alpha = \widetilde{\Psi}(z) \tag{2.2}$$

should be sparse or compressible.

The reconstruction process estimates the sparse coefficients set of some patch set covering the entire image of interest which is consistent with the object's system response. In particular, let $\{z_k\}$ be a patch set extracted from the original image x, the image of the object can be mathematically represented by its patches as

$$x = P(\{z_k\}), \tag{2.3}$$

where $P(\cdot)$ is an operator that combines the patch set to obtain the original image. Denote $\{a_k\}$ as the coefficients of the patches $\{z_k\}$ and $\Psi(\cdot)$ as the inverse sparsifying transform of $\widetilde{\Psi}$ satisfying $z_k = \Psi(\alpha_k)$ for all k, the sensing process can be written as

$$y = A\Big(P\big(\Psi\{\alpha_k\}\big)\Big). \tag{2.4}$$

We propose to obtain the sparse coefficients from the following optimization problem

$$\min_{\{\alpha_k\}} \sum_k ||\alpha_k||_1 \;\; \text{s.t.} \;\; y = A\Big(P(\Psi\{\alpha_k\})\Big). \tag{2.5}$$

This optimization problem can be solved efficiently by an iterative alternating minimization procedure. At iteration t of the algorithm, a noisy estimate $x^{(t)}$ of the original image consistent with the object's system response is reconstructed based on the information from the previous iteration. The estimates of the sparse coefficients $\{\alpha_k^{(t+1)}\}$ at this iteration can then be found by thresholding the coefficients of the noisy patches $\{z_k^{(t)}\}$ extracted from $x^{(t)}$. The error between the true measurements and the sparsified reconstruction with the known coded-aperture response is used to generate the next image estimate as $x^{(t+1)}$. The algorithm stops when a maximum number of iterations is reached or the inconsistency between the estimate and the measurements is sufficiently small.

2.3 Experimental System - Mk I

The calibration projector includes an incoherent light source (M530L3, MCWHL5 Thorlabs), an aspheric lens (lens 1, ACL5040U-A Thorlabs), a digital micromirror device (DMD, DLP3000, Texas Instruments), and an achromatic lens (lens 2, #49-664 Edmund Optics). Lens 1 is used to best collimate the incoherent light onto the DMD while lens 2 is used to image the mirrors of the DMD onto the sample plane with approximately 3.3 de-magnification. Lens 1,2 and

the DMD are used to project and scan a point source across the field-of-view of our sample plane. A DMD macro pixel is used to generate a square point source of 16.3-μm or 9.78-μm width. A 20× objective lens and a CCD camera (GS3-U3-15S5M-C, Pointgrey) are used to image the proximal end of the multicore fiber, which acquires the system responses of each point source and an object.
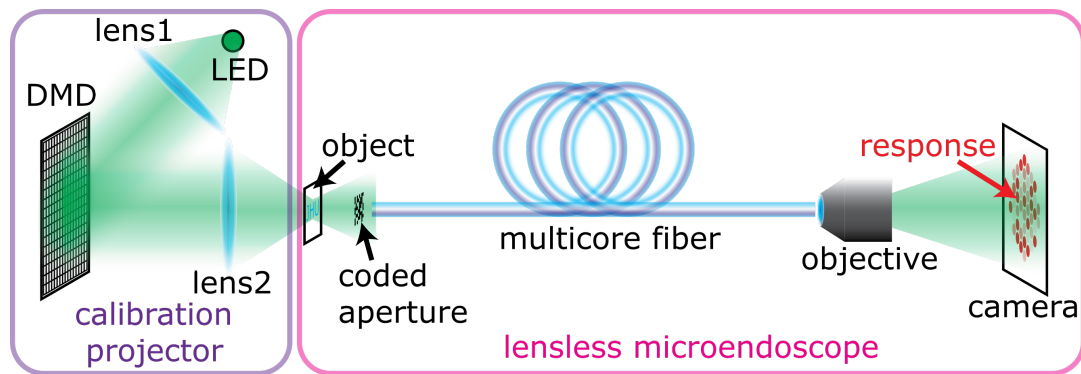
Figure 2.3: Detailed schematic of the coded-aperture-based computational microendoscope consisting of calibration optics and the imager.

Custom scripts were written to automate the data acquisition, which upload a macro pixel on the DMD, acquire a single snapshot from the camera, and repeat for every macro pixel generated across the sample plane. In addition to data acquisition, custom scripts were written to process the coded-aperture response images as we need to acquire the light intensities in each fiber core. A local maxima pursuit algorithm (median filter followed by convolution with a gaussian point spread function) is used to compute the spatial positions of the fiber cores from an image of the multicore fiber, and this core map is piecewise multiplied to every coded-aperture responses to extract the light intensities in

each fiber core. This process is repeated for every point source being generated which completes the calibration matrix. The same extraction process is done only once for the single-shot measurement of an object's coded-aperture response, and the image reconstruction algorithm is used to recover the object image.

2.3.1 Multicore Fiber and Coded-Aperture

The multicore fiber (FIGH-06-300S, Fujikura, distributed by Myriad Fiber Imaging in U.S) used to acquire all experimental data is a 30-cm-long multicore fiber consisting 6000 fiber cores with 3-μm core diameter, 3.3-μm core pitch, 270-μm image circle diameter, 300-μm fiber diameter, and 400-μm coating diameter. The coded-aperture used in the experiment has a minimum feature size of 10-μm, limited by our printing capabilities. The coded-aperture is laser-printed on a transparency and is a two-dimensional square-shaped, uniformly distributed pseudorandom binary pattern. Due to the feature size of the coded-aperture and the inherent cross talk in the multicore fiber, the distance between the mask and the fiber is set to be 1-mm with the imager's working distance being approximately 4-mm in order to ensure sufficient shift in the coded-aperture responses of each point source from the scene.

2.4 Experimental Results - Mk I

2.4.1 Lens-based versus Lens-free Microendoscope

Example experimental results of the imaging system are shown in Figure 2.4. For reference, images of projected test objects (Fig. 2.4 **A,B**) and a prepared

slide of esophagus tissue (Fig. 2.4 **C**) are acquired using a high resolution bulk microscope. The corresponding objects imaged through a conventional lens-based multicore fiber microendoscope are also shown (Fig. 2.4 **D,E,F**) by using a lens and the multicore fiber. Imaging results from our distal lensless system are demonstrated using a coded-aperture and the same multicore fiber and are shown (Fig. 2.4 **G,H,I**). Further more, their corresponding raw camera images used to reconstruct these images are shown (Fig. 2.4 **J,K,L**). Experimental results generated from **Mk I** system have a 980-μm-wide field-of-view.

2.4.2 Test for Spatial Resolution

Resolution targets are imaged (Fig. 2.5) in order to determine the spatial resolution of **Mk I** imaging system. Microscope images of the resolution targets (Fig. 2.5 **A,B,C**), images using the conventional lens-based multicore fiber microendoscope (Fig. 2.5 **D,E,F**), and the distal lensless microendoscope image reconstructions (Fig. 2.5 **G,H,I**) are shown. The linewidths in Figure 2.5 **A,D,F** are 44-μm, 40-μm, and 33-μm respectively, the linewidths in Figure 2.5 **B,E,F** are 32-μm, 29-μm, 26-μm, and 22-μm respectively, and the linewidths in 2.5 **C,F,I** are 21-μm, 19-μm, 17-μm, and 14-μm respectively. Unlike lens-based approach, lensless imaging is capable of resolving 14-μm features as shown in Figure 2.6.

2.4.3 Dynamic Scene Reconstruction

Interestingly, the imaging architecture presented here is comparable to the single-pixel camera shown in 1.7, where each measurement carries global

	Object	Lens-based Imaging	System Response	Lensless Imaging
	A	D	G	J
	B	E	H	K
	C	F	I	L
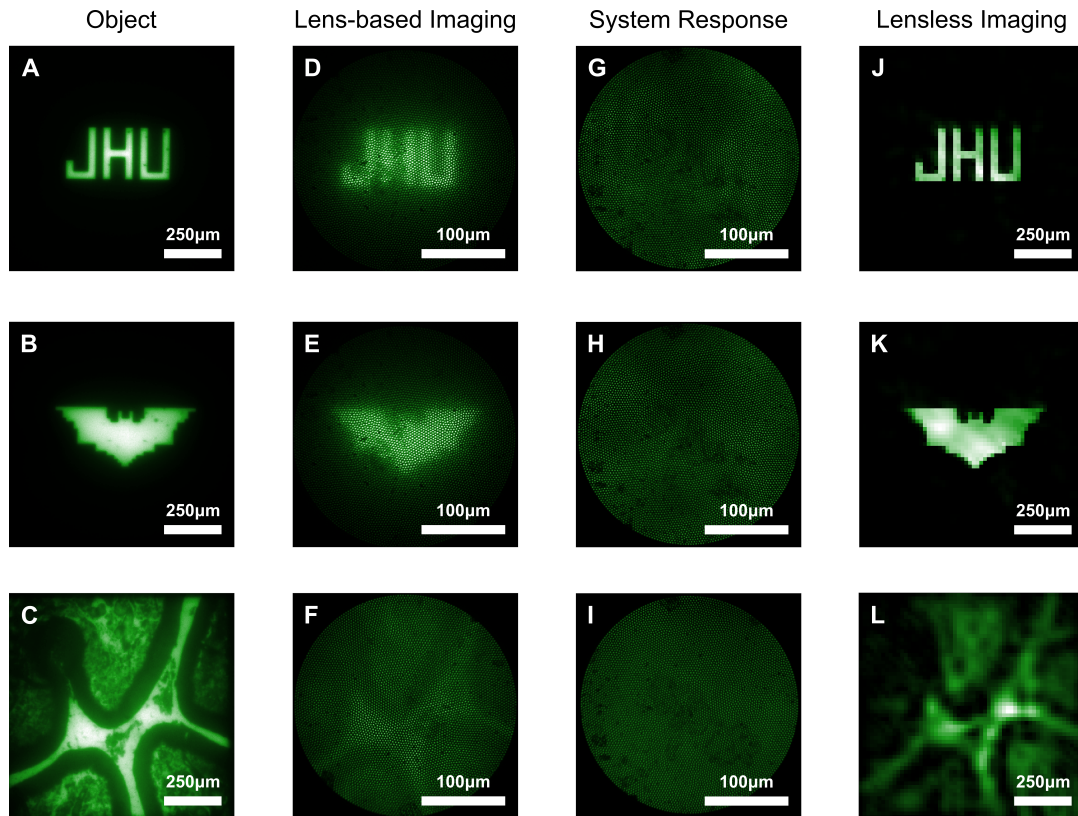
Figure 2.4: Experimental imaging results. **(A)-(C)** Object images acquired using a bulk microscope. Experimental results shown throughout have a 980-μm-wide field-of-view. **(D)-(F)**, Objects imaged using a conventional lens-based multicore fiber microendoscope. Scene is de-magnified to fit within the fiber's image circle diameter of 270-μm. **(G)-(I)**, Raw images captured from the proximal end of the multicore fiber in our distal lensless microendoscope employing a distal coded-aperture and used to reconstruct **(J)-(L)**. Objects imaged using our distal lensless microendoscope are shown in **(J)-(L)**.
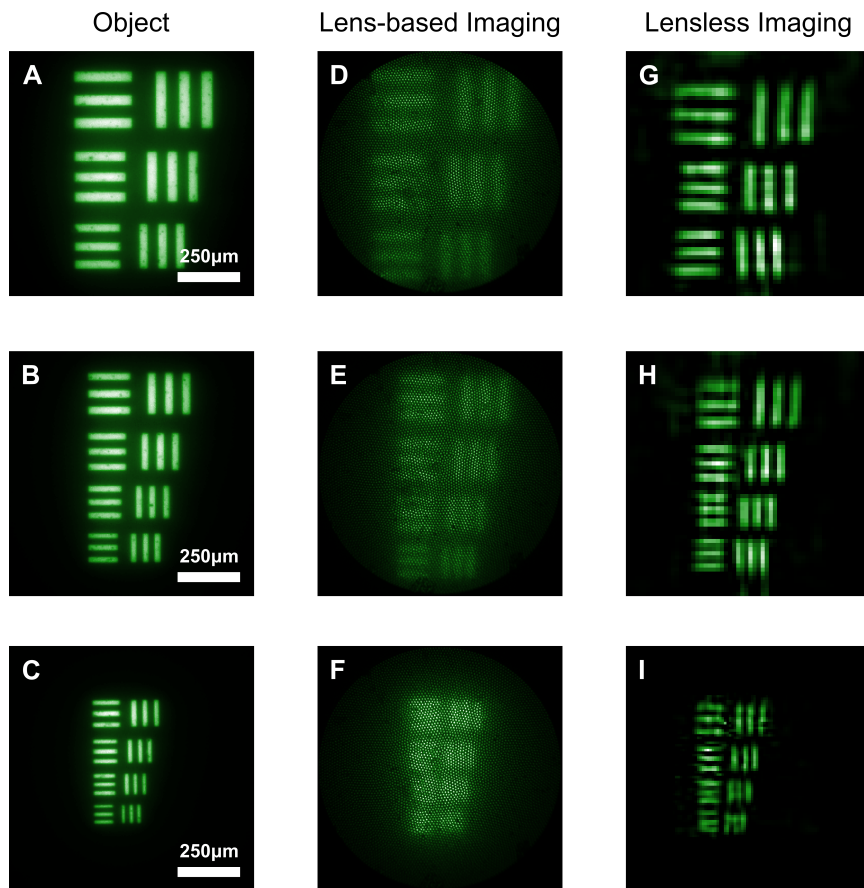
Figure 2.5: Test for lateral resolution. **(A)-(C)** Images of the resolution target objects acquired using a bulk microscope. **(D)-(F)** Objects imaged using a conventional lens-based multicore fiber microendoscope. **(G)-(I)** Objects imaged using our lensless multicore fiber microendoscope employing a distal coded-aperture. **(A)(D)(G)** widths of the lines are 44-μm, 40-μm, and 33-μm. **(B)(E)(H)** widths of the lines are 32-μm, 29-μm, 26-μm, and 22-μm. **(C)(F)(I)** widths of the lines are 21-μm, 19-μm, 17-μm, and 14-μm.
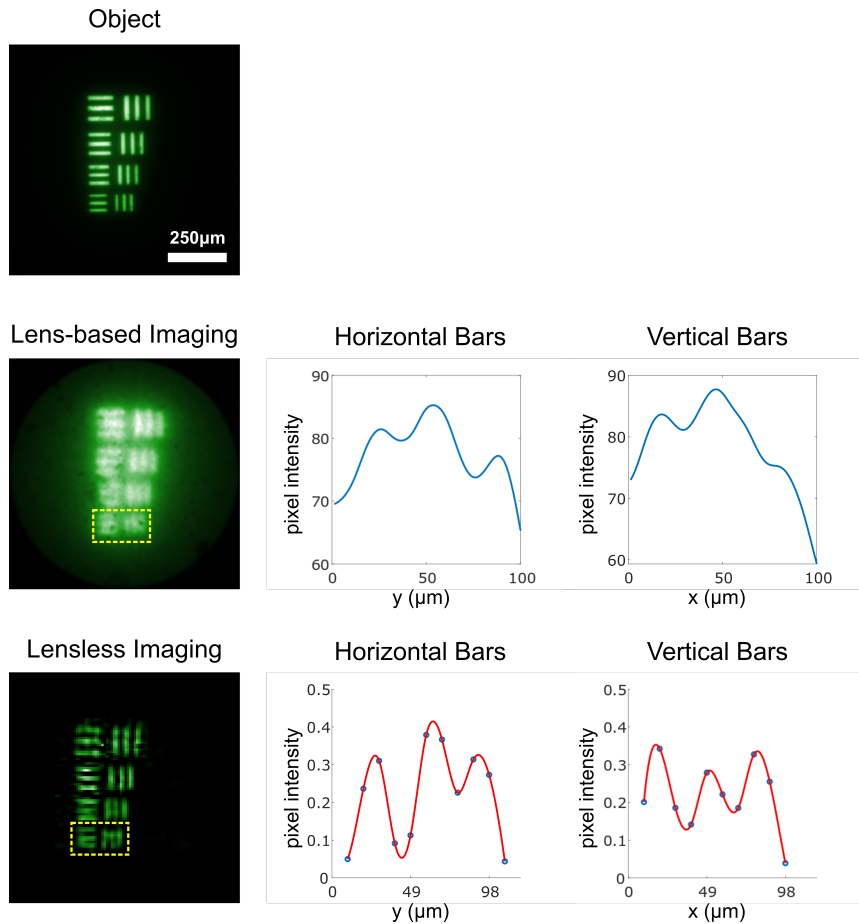
Figure 2.6: Comparison of lateral resolution between lens-based and lensless multi-core fiber microendoscopes. Above results shown resolution targets with linewidths 21-μm, 19-μm, 17-μm, and 14-μm. Lens-based image of the resolution targets is lowpass filtered in order to remove the pixelation artifacts due to fiber cores. Regions of interest (yellow dotted lines) show 14-μm linewidths and is used to generate the average horizontal and vertical intensity variations. Line fitting (red curve) in addition to pixel values (blue dots) is used for lensless imaging result, and show that 14-μm linewidths are resolved by the Rayleigh criterion.

information about the scene [17]–[20]. However, contrary to single-pixel cameras that sequentially mask the scene with varying spatial patterns and acquire each measurement sequentially, our imaging system only requires a single pseudorandom spatial mask and acquires the spatially-multiplexed measurements from a single camera frame, and is therefore highly suitable for capturing dynamic scenes. To demonstrate this we experimentally reconstruct a time-varying scene acquired at the native frame rate of our camera (50 frames per second), and is shown in Figure 2.7. The pixel resolution of the camera does not dictate the frame rate of the lensless microendoscope, provided enough pixels are available to measure the light intensity in each fiber core. For calibration and imaging, we acquire images of the fiber cores using only 10 camera pixels per core. Given the modest pixel requirements of the present system, we anticipate th signal-to-noise of the system response to be the primary limiter of the maximum frame rate, not the camera data throughput.

2.4.4 Volumetric Reconstruction

A dramatic benefit of the lensless microendoscope system presented is the ability to computationally refocus on objects that are positioned at different depth without any actuated components and using only a single camera frame. Conventionally, optical endoscopes with depth scanning capabilities require components capable of physically varying the focal plane, such as an electrically tunable lens, which makes brain mounting of freely moving animals difficult due to increased distal footprint and weight [29]–[32]. In stark contrast to these bulky approaches, we can simply calibrate the system
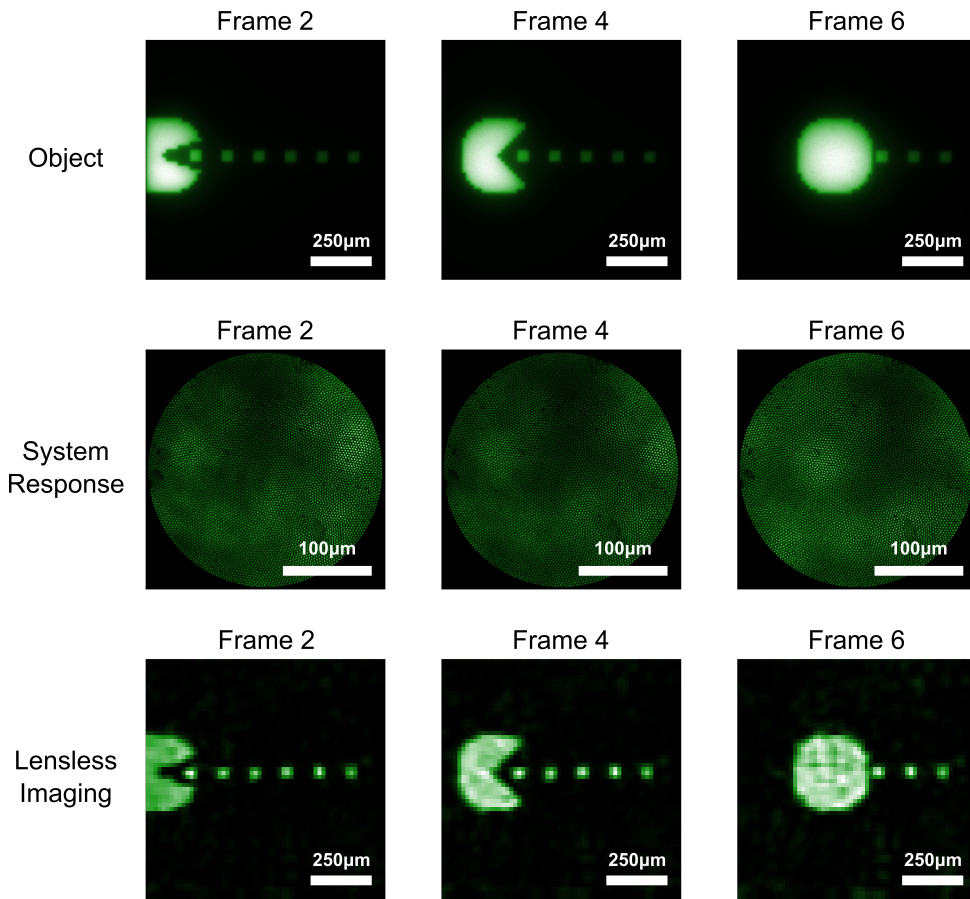
Figure 2.7: Demonstration of time-varying scene reconstruction. A moving object is generated using the DMD from Figure 2.3 and imaged using a lens and a camera. The lensless microendoscope system responses for different frames are acquired at 50 frames per second using the CCD camera and used to reconstruct the scene.

responses at different depths and reconstruct the scene volumetricaly without actuation from a single camera snapshot. As a demonstration of this, Figure 2.8 **A,B** shows the microscope images of two test objects separated in depth by 1.5-mm. Using a single snapshot (Fig. 2.8 **C**), we can volumetrically reconstruct an image volume of the objects and digitally focus on either objects (Fig. 2.8 **E,F**) simply by choosing the depth plane within the reconstructed volume. Experimentally, this volumetric reconstruction of the scene is enabled by the calibration of 11 depth layers separated by 300-μm in depth. In the present configuration, the lensless microendoscope demonstrates an axial resolution of approximately 300-μm as shown in Figure 2.9.
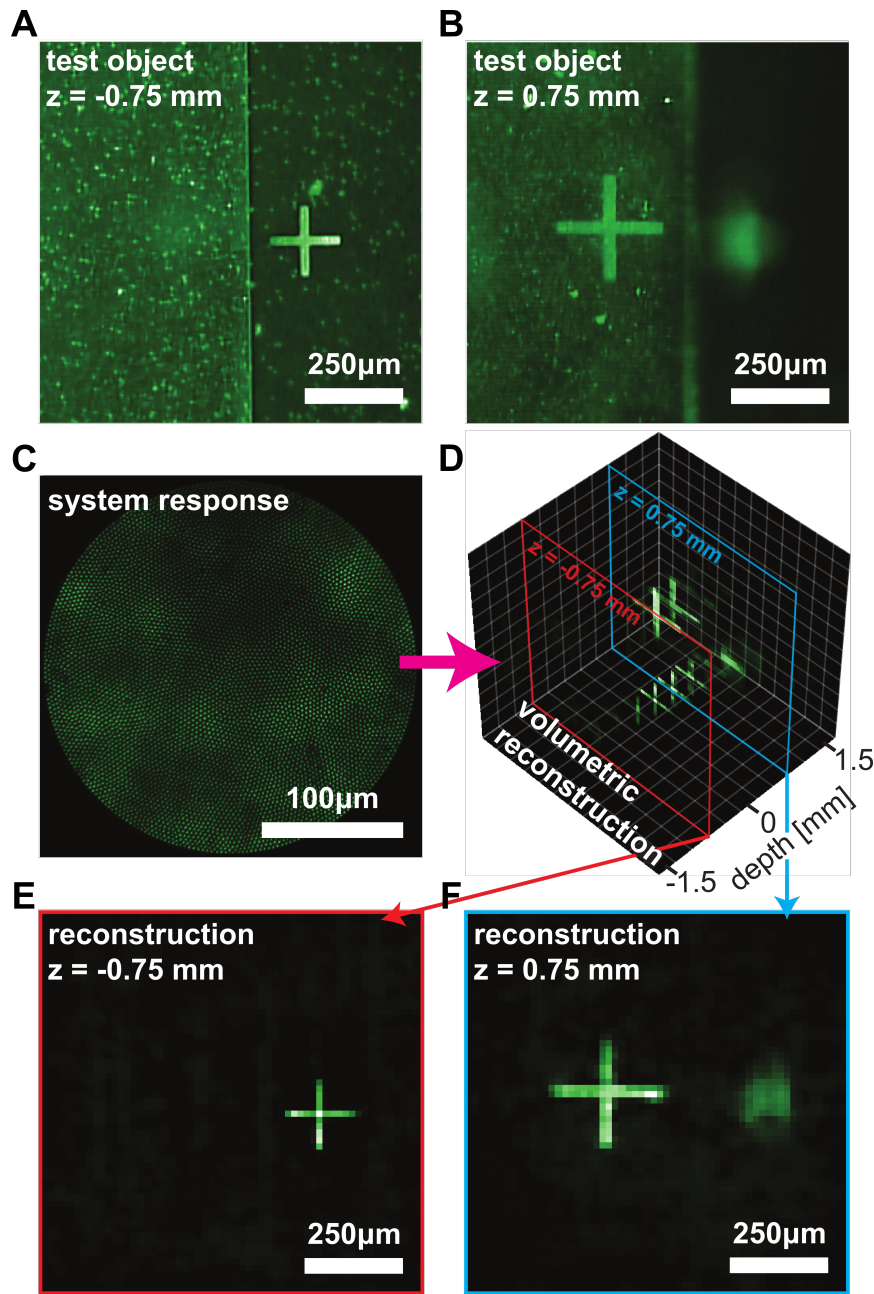
Figure 2.8: Volumetric reconstruction and computational refocusing. **(A)(B)** Bulk microscope images of the test subject which consists of two planar objects separated in depth by 1.5-mm. The image volume is reconstructed from a single image of the multicore fiber's proximal end, shown in **(C)**. **(D)** shows volumetric reconstruction with 11 depth layers, separated in depth by 300-μm, using the system response shown in **(C)**. **(E)(F)** images from the volumetric reconstruction corresponding to the two depths that the objects are in the best focus.
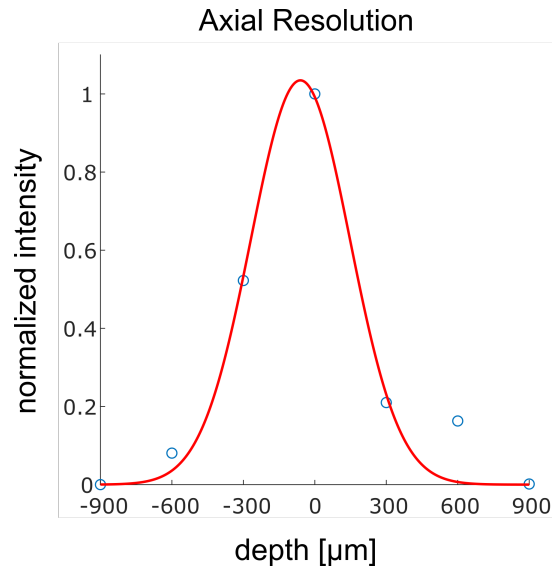
Figure 2.9: Determining the axial resolution of the lensless microendoscope. An experimental point source is reconstructed at different depths and the corresponding intensity fall-off is recorded as a function of depth. A fitted Gaussian curve shows that the axial resolution is approximately 300-μm according to the Rayleigh criterion.

2.4.5 Color Imaging

Beyond computational refocusing this lensless approach can also achieve color imaging without any additional components. In contrast, microlens-based systems suffer from significant chromatic aberrations that are difficult to correct. Using the proposed lensless approach, one can simply employ a color camera and calibrate the sensing matrix for each color channel resulting in no chromatic aberration, in principle. To demonstrate this color imaging capability a white light LED is used as the light source and we reconstructed and overlay images of each color channel to generate the results shown in Figure 2.10.
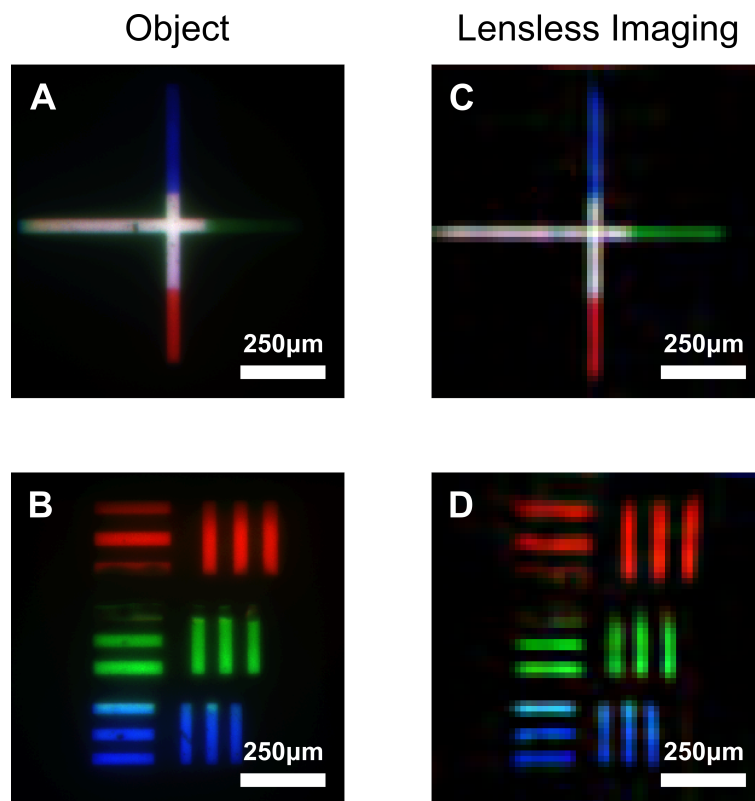
Figure 2.10: Demonstration of color imaging. **(A)(B)** Images of multi-color objects acquired using a bulk microscope. **(C)(D)** Color image reconstructions of the same objects using our lensless microendoscope.

2.4.6 Insensitivity to Fiber Bending

Figure 2.11 shows the system responses of a point source used in the calibration, both with bending and without bending of the fiber. The 30-cm-long multicore fiber is bent approximately 30° from its normal axis. The light intensities in each fiber core are extracted for both fiber deformations, shown in the bottom Figure. The correlation between the two measurements is 0.99, demonstrating high repeatability and lack of bend sensitivity.

2.5 Information Capacity

Have we really increased the information capacity of a microendoscope using a coded-aperture and computational imaging techniques? Below analysis shows that we have indeed increased the information content by three-fold for a single depth plane. Notably, the ability to reconstruct a volume from a single camera snapshot even further increases the space-bandwidth product (SBP) of the lensless system. The specs of the lens-based and lensless microendoscopes are summarized in below table.

The lateral resolution of the lens-based microendoscope is the best-case theoretical resolution (ignoring crosstalk, optical aberration in microlens, etc) which meets the Nyquist requirement of two fiber cores per resolution element [42]. In other words, the lens-based multicore fiber with $3.6\times$ de-magnification can resolve a minimum feature size of $3.6 \times 2 \times (3.3\text{-}\mu\text{m core pitch}) = 24\text{-}\mu\text{m}$. Direct calculation of the SBP is the following: $\frac{\text{field-of-view}}{\text{Nyquist resolution}} = \frac{0.754 \text{ mm}^2}{(12 \ \mu\text{m})^2} =$
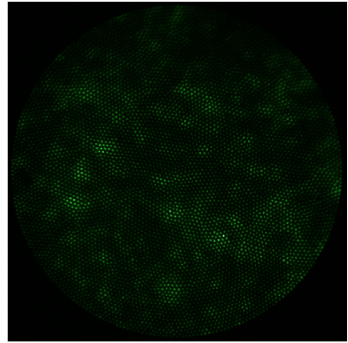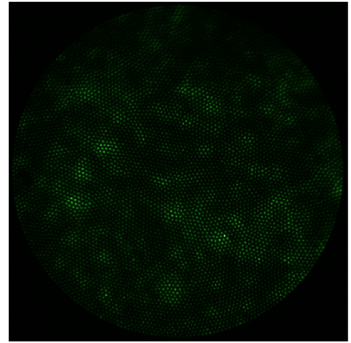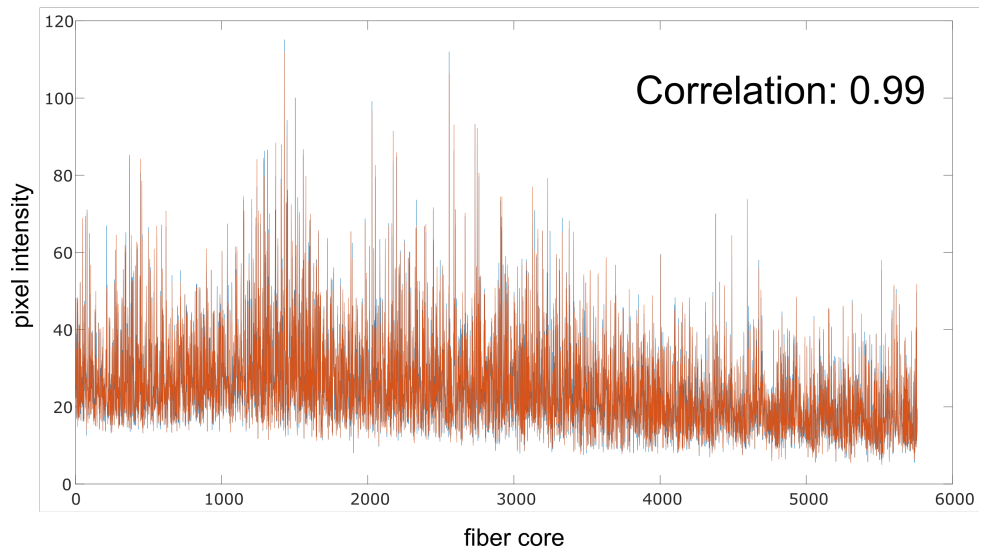
Figure 2.11: Demonstration of insensitivity towards bending of the multicore fiber of the lensless microendoscope.

5236. This calculation is in good agreement with the theoretical SBP in the lens-based microendoscope, which is the total number of fiber cores (6000 cores) in the multicore fiber. In comparison, the SBP in the lensless microendoscope is $\frac{0.96 \text{ mm}^2}{(7 \text{ } \mu\text{m})^2} = 19592$ for a single depth plane.

	Lens-based	Lensless
FOV	0.754 mm²	0.960 mm²
Lateral Resolution	24 μm	14 μm
2D Space-Bandwidth Product	6000	19592
Depth Resolution	N/A	300 μm
Video Frame Rate	50 fps	50 fps

2.6   Experimental System - Mk II

Above sections have demonstrated a lensless computational microendoscope with capabilities and performance that are not possible with conventional lens-based microendoscopes. However, there are several design mechanisms to be addressed before transitioning to real-time imaging of freely-behaving animals. First is to ensure the fluorescence imaging capability where the multicore fiber is used to simultaneously deliver light to a scene and collect the excited fluorescence emission. Another requirement is the appropriate design of the amplitude mask (i.e. coded-aperture) that casts the smallest features on the distal end while preserving the decorrelation of each point source, which would maximize the lateral and axial resolutions. In addition, it is advantageous to set the working distance of the microendoscope in hundreds of μm in order to avoid scattered light from the animal brain tissue.

The following presents the next generation of the coded-aperture-based computational microendoscope that meets the above requirements. Notably, a

coded-aperture with high modulation contrast is fabricated using photolithographic techniques, and is UV-glued to the distal end of the multicore fiber. The coded-aperture used in the following experiment has a minimum feature size of 7-μm, while the distance between the amplitude mask and the fiber is set to be 500-μm with the imager's working distance being approximately 400-μm. In **Mk II** the multicore fiber is used to both illuminate the scene and collect the fluorescence emission (epi-fluorescence), and the corresponding system response is used to reconstruct the scene and digitally refocus to fluorescent objects located at varying depths.

Figure 2.12 **(A)** presents the epi-fluorescence computational microendoscope. The light from a continuous-wave laser (Verdi G7, $\lambda = 532$nm, Coherent Inc.), aspheric condenser lens (ACL5040U, Thorlabs), and a $10\times$ objective lens are used to fully couple into the 6000 fiber cores in the multicore fiber (FIGH-06-300S, Fujikura). The light at the distal end propagates from the cores through the coded-aperture, and evenly illuminates the scene. A rotating ground-glass diffuser is employed to eliminate the coherence of the laser light. Note that the imaging system does not rely on spatial or temporal coherence: the CW laser is only used to excite the fluorescent objects in the scene and thus the imaging system is still insensitive to bending of the multicore fiber. The fluorescent light from an unknown object propagates from the scene through the coded-aperture, and is collected by the same multicore fiber. The $10\times$ objective lens and a camera (GS3-U3-15S5M-C, Pointgrey) are used to image the proximal end of the multicore fiber and thus acquire the system reponse of the unknown object. A long-pass dichroic mirror (DMLP550, Thorlabs) and

(A) Lensless Microendoscope

laser

rotating diffuser

lens

filter

object

coded aperture

multicore fiber

objective

dichroic mirror

camera
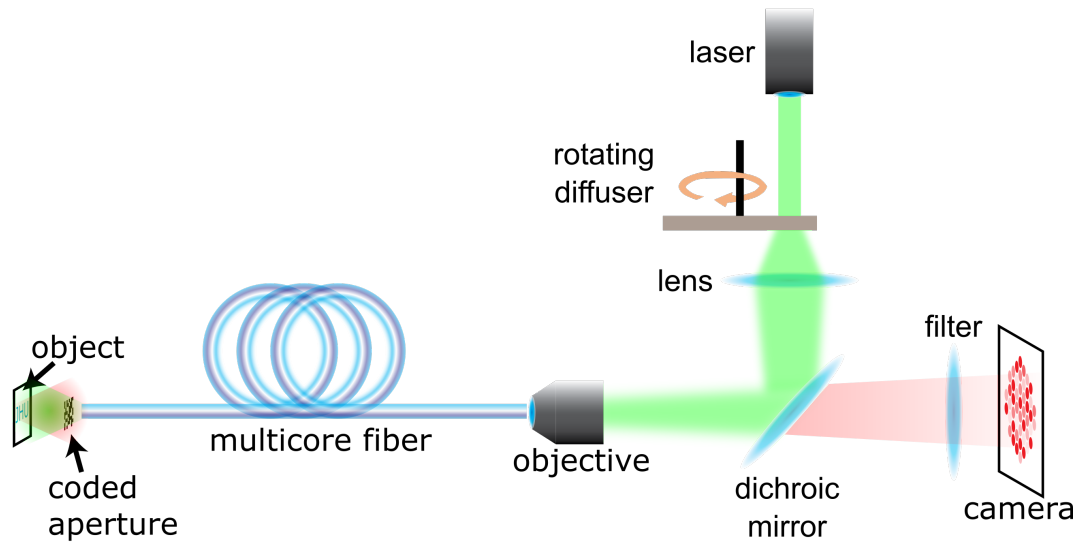
(B) Calibration Module

pinhole

LED

diffuser
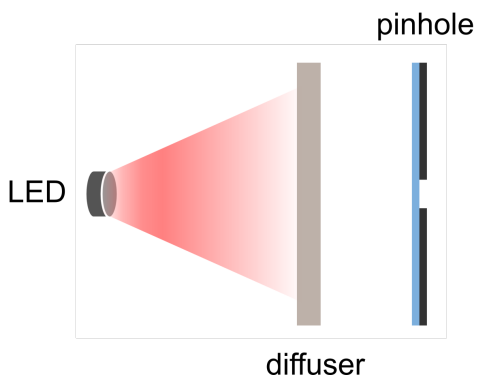
Figure 2.12: Detailed schematic of the imaging system consisting of the calibration module and the lensless microendoscope.

a filter (FEL0550, Thorlabs) are employed to sufficiently reject the excitation light from the fluorescence emission.

Figure 2.12 **(B)** shows the side view of the calibration module consisting of an LED (M565L3, Thorlabs) with the central wavelength that matches the peak fluorescence emission, a ground-glass diffuser (DG10-1500, Thorlabs), and a 5-μm-wide spatial pinhole (P5D, Thorlabs). The calibration module is mounted on a motorized xy-stage and a manual z-stage to calibrate for a volumetric scene. Custom scripts are written to automate the data acquisition, which positions the spatial pinhole in an xy-coordinate, acquire a single snapshot from the camera, and repeat for every xyz-position across the scene with 5-μm and 10-μm pitch. Identical scripts from **Mk I** system are used to build the calibration matrix and process the single-shot measurement of a fluorescent object's coded-aperture response. Previously described patch-based iterative optimization algorithm (2.2) is used to reconstruct images of 10-μm fluorescent particles (Nile Red, Spherotech).

2.6.1   Coded-Aperture Fabrication

Figure 2.13 shows the steps taken to fabricate the coded-aperture via photolithography. A fused silica wafer is the substrate of choice since it has a good transmission in the visible wavelength and low thermal expansion. The wafer thickness is set as 500-μm which determines the distance between the coded-aperture and the distal end of the multicore fiber. The wafer is deposited with 100-nm-thick chromium and covered with photoresist via spin-coating. A photomask (i.e square-shaped, uniformly distributed pseudorandom binary
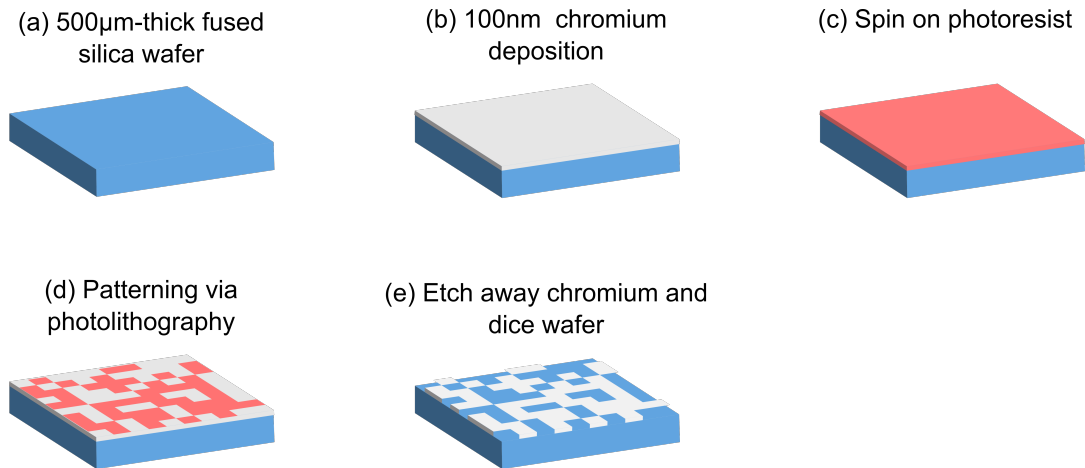
Figure 2.13: Fabrication of the amplitude mask and spacer.

pattern) is aligned and exposed to UV light to pattern the photoresist. Consequently, chromium is liquid-etched away, remaining photoresist are removed, and the wafer is diced to appropriate dimensions to be UV-glued to the distal end of the multicore fiber. Figure 2.14 shows the microscope image of the fabricated coded-aperture with 7-μm minimum feature size.

2.7 Experimental Results - Mk II

2.7.1 Lensless Epi-Fluorescence Imaging

Experimental results demonstrating the fluorescence compatibility are shown in Figure 2.15. For reference, ground truth images of the fluorescent particles (Fig. 2.15 **A,B**) are acquired using a high resolution bulk microscope, where **(B)** is the magnified image of the yellow region-of-interest displayed in **(A)**. The respective widths of the two field-of-views shown throughout the experimental results are 320-μm and 640-μm. Imaging results from the lensless microendoscope are shown in Figure 2.15 **(D)(E)**. Furthermore, the
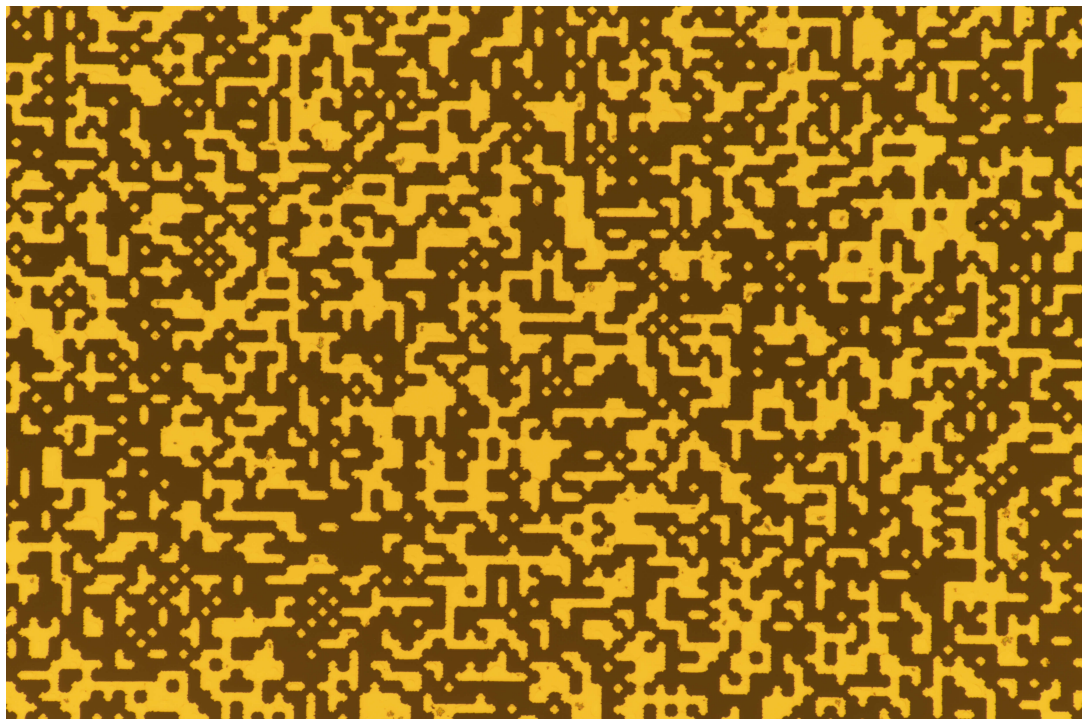
Figure 2.14: Microscope image of the coded-aperture fabricated using photolithographic techniques. The amplitude mask is a square-shaped, uniformly distributed pseudorandom binary pattern with 7-μm minimum feature size.

Widefield Fluorescence

System Response

Lensless Imaging
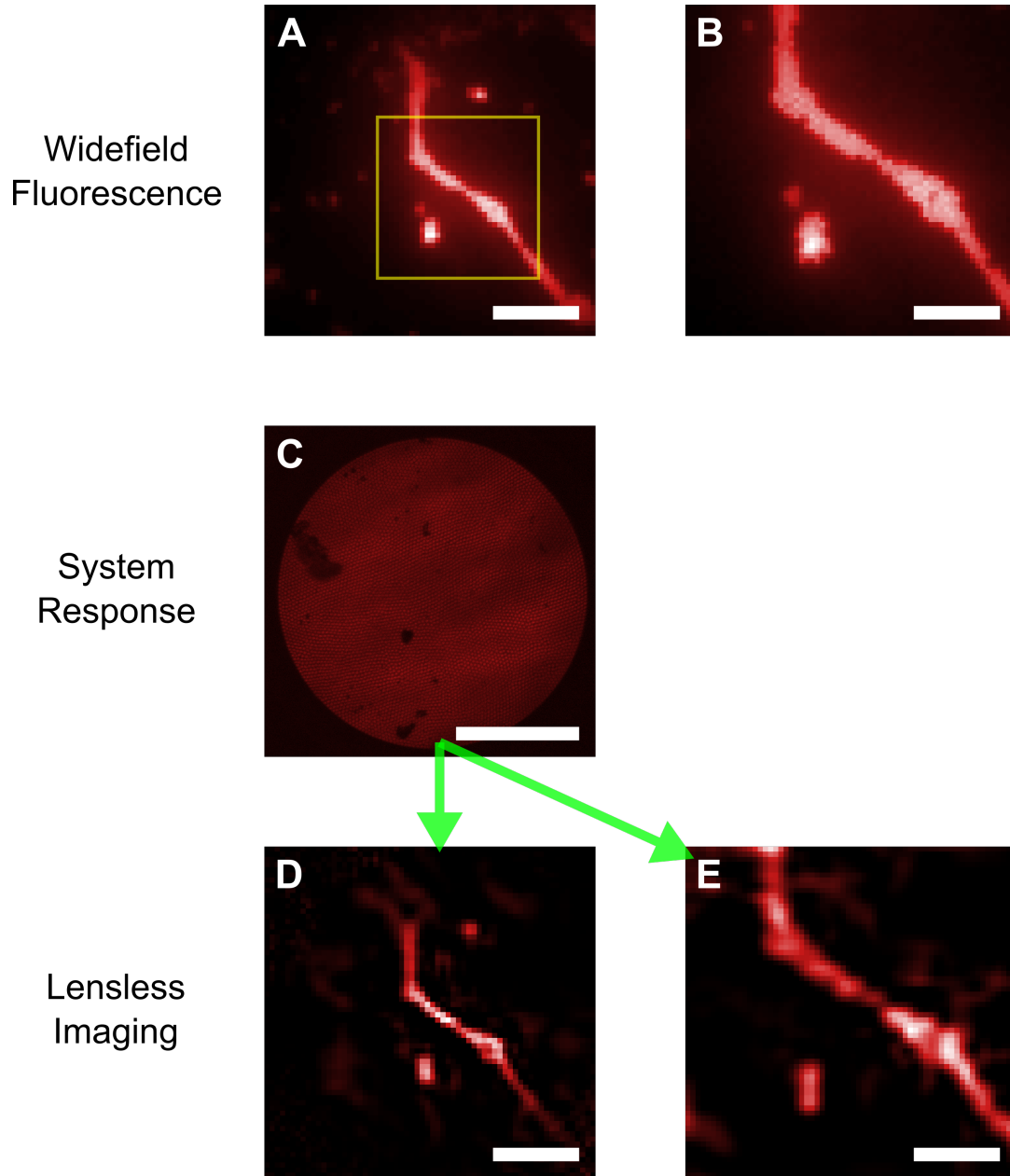
Figure 2.15: Experimental imaging results. **(A)(B)** Ground truth images of 10-μm fluorescent particles acquired using a bulk microscope. **(C)** Raw image of the system response captured from the proximal end of the multicore fiber that is used to reconstruct **(D)(E)**. Scale bar = 200-μm (**A,D**) and 100-μm (**B,C,E**).

corresponding raw camera image used to reconstruct these images are shown in Figure 2.15 **(C)**.

2.7.2 Digital Refocusing

Experimental results demonstrating the computational refocusing capability of the lensless microendoscope is shown in Figure 2.16 and 2.17. A simple calibration of the system responses at different depths enables the volumetric reconstruction of the scene from a single camera snapshot. Figure 2.16 **(A)(B)** show the microscope images of two fluorescent particle clusters that are separated in depth by approximately 250-μm. Figure 2.17 **(A)(B)** are the magnified images of the yellow region-of-interest displayed in 2.16 **(A)(B)**. Using a single snapshot (Fig. 2.16 **C**) we can digitally focus on either clusters (Fig. 2.16 **D,E** and Fig. 2.17 **C,D**) simply by choosing the depth plane within the reconstructed volume.

2.8 Discussion and Future Work

In summary, I have demonstrated a distal lensless, scan-free microendoscope using a coded-aperture at the distal end of a multicore fiber. By replacing distal lenses with a single spatial mask, widefield images of the scene are computationally recovered with superior image quality to a comparable conventional lens-based approach. Also, the imaging system is capable of computational refocusing of objects separated in depth without actuation using a single snapshot of the scene's coded-aperture response. Furthermore, the presented
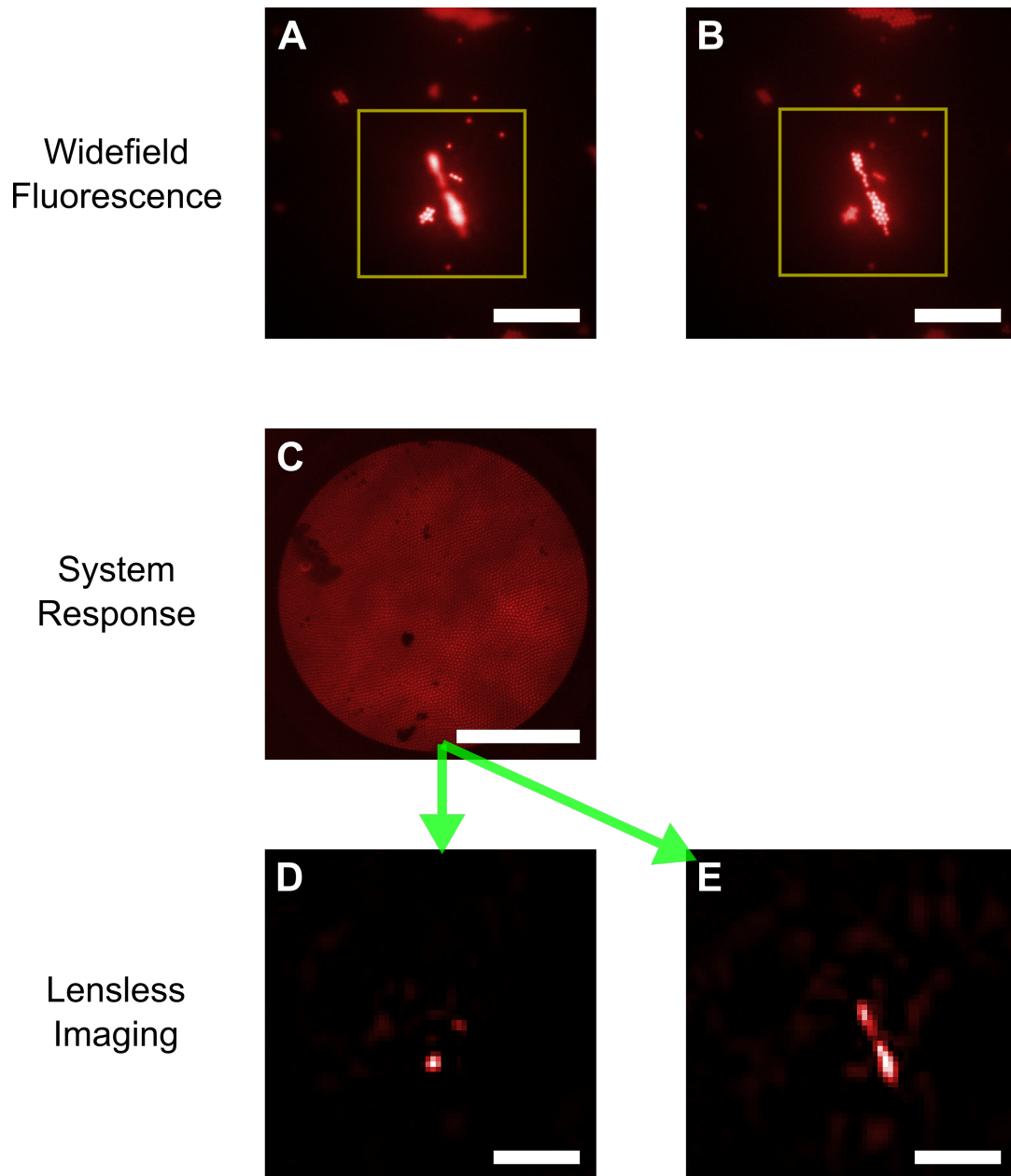
Figure 2.16: Computational refocusing. **(A)(B)** Bulk microscope images of two 10-μm fluorescent particle clusters that are separated in depth by 250-μm. The volumetric scene is reconstructed from a single image of the multicore fiber's proximal end, shown in **(C)**. **(D)(E)** Reconstructed images from the lensless microendoscope corresponding to the two depths that the two clusters are in best focus. Scale bar = 200-μm (**A,B,D,E**) and 100-μm (**C**).

Widefield Fluorescence

Lensless Imaging
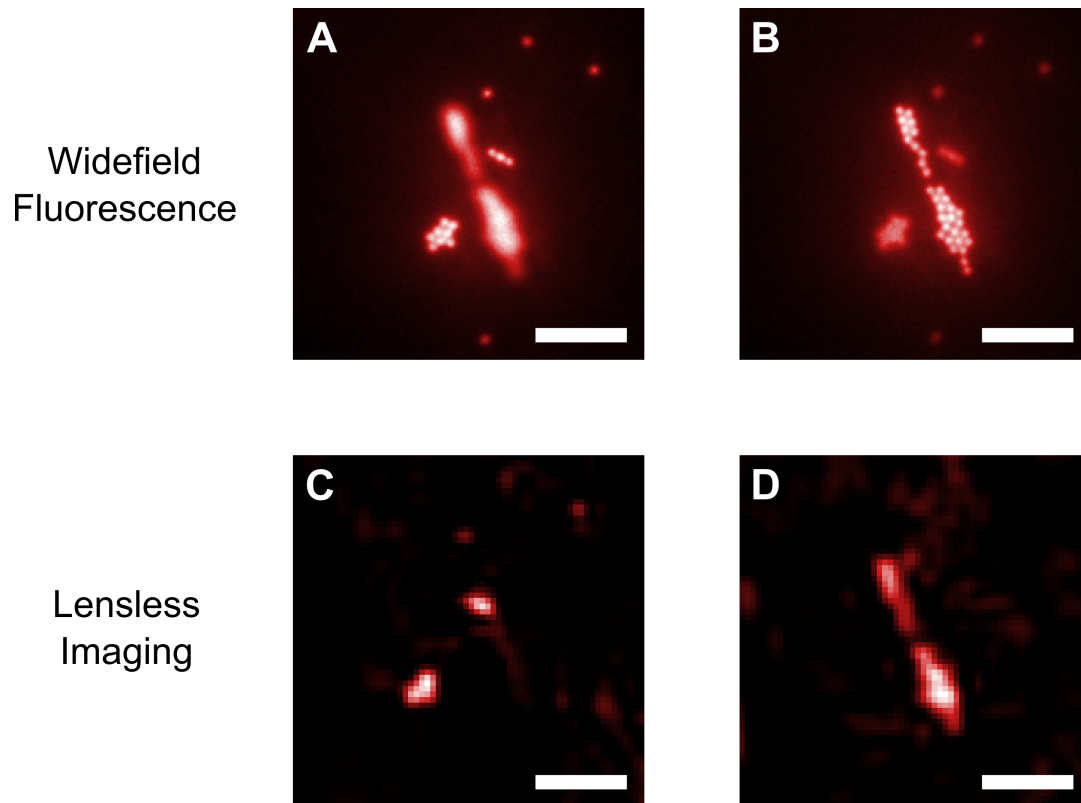
Figure 2.17: Computational refocusing. **(A)(B)** Magnified bulk microscope images of the yellow region-of-interest displayed in 2.16 **(A)(B)**. Volumetric scene is reconstructed from a single image of the multicore fiber's proximal end, shown in 2.16 **(C)**. **(C)(D)** Reconstructed images from the lensless microendoscope that digitally focuses on the two fluorescent particle clusters separated in depth by 250-μm. Scale bar = 100-μm.

technique does not require additional elements to correct for chromatic aberrations, enabling color imaging by simply calibrating for each color channel. Future improvements on this work will include optimizing the minimum feature size of the pseudorandom amplitude mask and its distance from the multicore fiber through wave diffraction simulation. Furthermore, polishing the amplitude mask down to the diameter of the multicore fiber is highly desired in order to further minimize the invasiveness of the microendoscope. Lastly, an image reconstruction algorithm that leverages the temporal sparsity would be very beneficial in recovering a time-varying scene, such as firings of neurons. Overall, the presented imaging system demonstrates an alternative design to ultra-thin microendoscopy with great potential for applications that demand extremely small and agile probes such as real-time imaging of neural activity in freely moving animals.

Chapter 3

Fluorescence Imaging Using Spatially-Dependent Scattering

This chapter presents a compressive imaging architecture employing a multi-core fiber with a cheap and readily available scattering distal tip. Unknown fluorescent objects are illuminated with randomly structured speckle patterns generated by a coherent light separately coupled through each fiber core to a ground glass diffuser at the distal end. Using the characterized speckle patterns and the total light collected from the object, we can computationally recover pixelation-free object images with up to seven times higher space-bandwidth product (SBP) than the number of fiber cores. Notably, the proposed imaging system is insensitive to bending of the fiber and extremely compact, making it suitable for minimally-invasive microendoscopy.

3.1   Harnessing Disorder for Imaging

Recent research has focused on using natural scattering media for improved image acquisition, including super-lenses, imaging around corners, blind
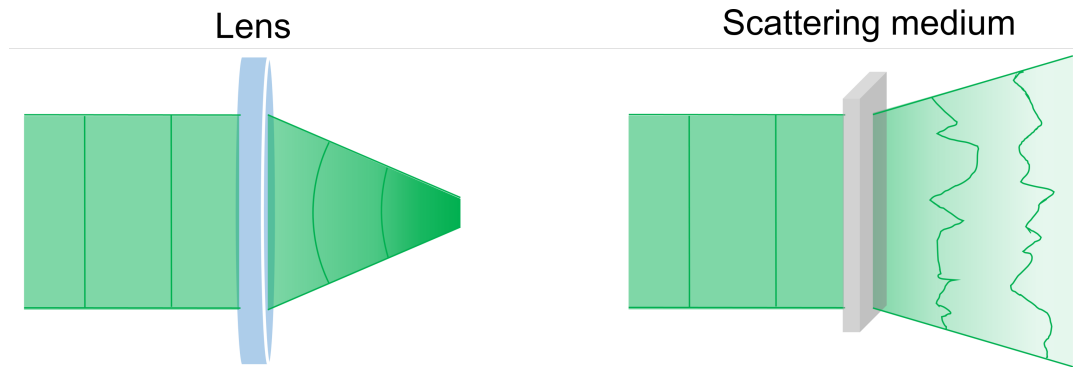
Figure 3.1: Illustration showing the different effects on the incident wavefront by a typical lens and a scattering medium. A typical lens applies a quadratic phase shift on the incident wavefront, and thus focuses it to the smallest possible spot. A scattering medium applies a random phase profile on the incident wavefront which generates a complex spatial interference at the far-field.

structured illumination microscopy, and single-fiber imaging [43]–[49]. Complex spatial interference patterns known as "speckle" patterns are generated when a coherent source illuminates a scattering objects. Common scattering materials include paper, white paint, rough surfaces, or any media that has a large number of scattering particles. Such random patterns show great potential for imaging, as they have diffraction-limited speckle granules, allow for large spatial frequency content, and are easily and inexpensively generated. As shown in previous chapters minimally-invasive imaging tools have limited information capacity due to its given cross-sectional area. Specifically, the space-bandwidth product of a multicore fiber-based microendoscope is purely limited by the number of fiber cores. Thus, it is a natural progression to employ a scattering medium, which is capable of transmitting unprecedented amount of information, to increase the information capacity of a multicore fiber. However, the main challenge is designing the system that can harness

this disorder for imaging, as the complex and random nature of speckle patterns do not directly result in any image pixel information. Rest assured, the following experimental findings show that compressive imaging theory can be implemented to achieve such task.

Here, we present a minimally-invasive imaging approach that senses an unknown scene using spatially-encoded speckle patterns as shown [49] in Figure 3.2. Similar to a conventional raster-scanning microendoscope, we sequentially illuminate each fiber core in a multicore fiber. The light exiting the distal end propagates through a ground glass diffuser and, using up to 1000 cores, we generate up to 1000 unique speckle patterns to sense an unknown object. A single photodetector is used to collect the total light off the scene, which optically-computes the inner products between the patterns and the object. Using the characterized speckle patterns and the series of single photodetector measurements, we reconstruct images with an SBP of 2100 from between 300 and 1000 measurements (i.e., fiber cores) using a total variation (TV) minimization algorithm.

3.2   Mathematical Model

Let M and N represent the number of compressed measurements (i.e. fiber cores) and the pixel dimensions of the object image ($N = n_1 \times n_2$), respectively.
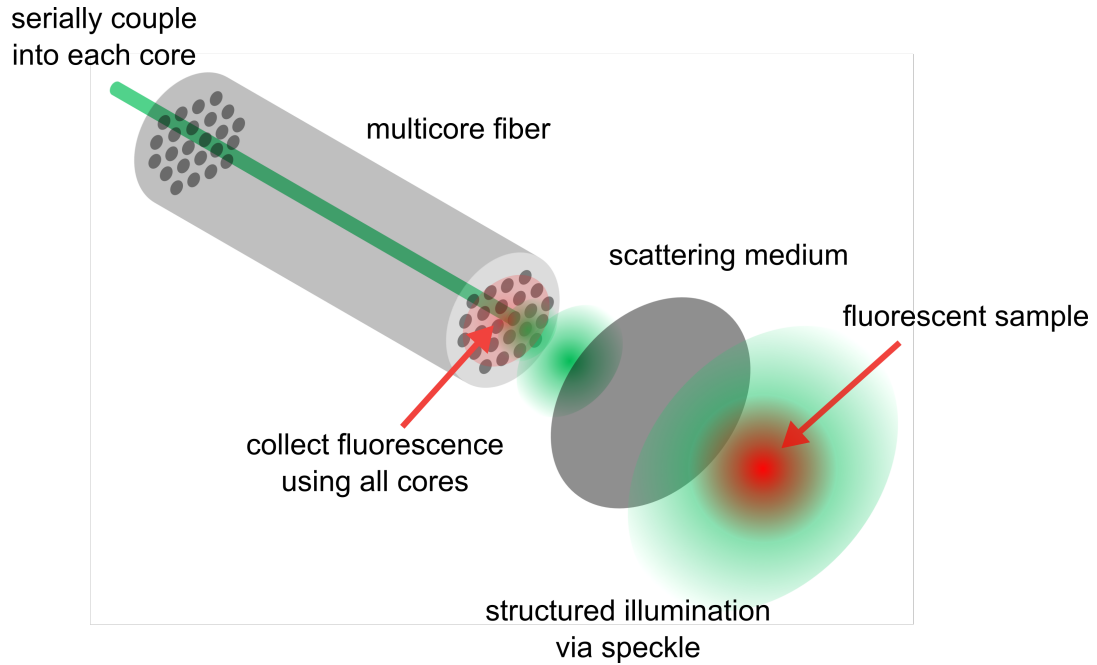
Figure 3.2: Conceptual illustration of the computational microendoscope using a multicore fiber with a distal scattering tip.

Figure 3.3: Illustration of discrete spatial gradient transform. Lena Image **(A)** is sparsity-transformed to the discrete gradient domain **(B)** which highlights the regions of rapid intensity change.

The observation vector $y \in \Re^{M \times 1}$ can be expressed as follows:

$$y = Ax = \begin{bmatrix} A_1 x \\ A_2 x \\ \vdots \\ A_M x \end{bmatrix} \tag{3.1}$$

where $A_1, A_2, ..., A_M \in \Re^{1 \times N}$ are the vectorized speckle patterns generated from each fiber core and a ground glass diffuser and $x \in \Re^{N \times 1}$ is the vectorized object image to be recovered. The sensing matrix A consists of M random illumination patterns vertically concatenated where $A \in \Re^{M \times N}$. For image reconstruction we assume that the object is sparse in the spatial gradient domain as illustrated in Figure 3.3. The spatial gradient of an image X of dimensions n_1 by n_2 is

$$g_{i,j} = \sqrt{(x_{i,j} - x_{i+1,j})^2 + (x_{i,j} - x_{i,j+1})^2} \tag{3.2}$$

where $x_{i,j}$ is the $\{i, j\}$th pixel intensity of X. The total variation (TV) norm is defined as the summed magnitude of the spatial gradient:

$$||x||_{TV} = \sum_{i=1}^{n_1} \sum_{j=1}^{n_2} g_{i,j}. \tag{3.3}$$

In turn, we can recover the image of our object by solving the following optimization problem:

$$\min_x ||x||_{TV} \ \text{s.t.} \ ||y - Ax||_2 \leq \sigma, \ x \geq 0. \tag{3.4}$$

where σ is a noise boundary. TV Minimization by Augmented Lagrangian

and Alternating Direction Algorithm [50] is used to reconstruct the image.

3.3 Experimental System
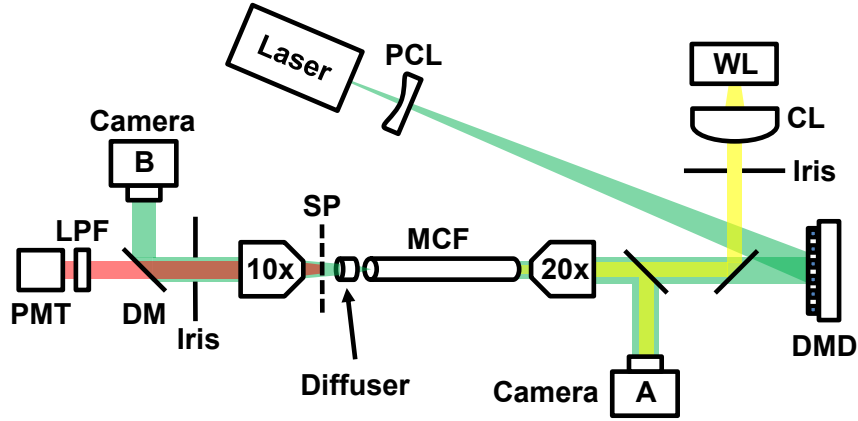
Figure 3.4: Experimental setup. WL = white light source, CL = condenser lens, DMD = digital micromirror device, PCL = plano-concave lens, MCF = multicore fiber, SP = sample plane, DM = dichroic mirror, LPF = long pass filter, PMT = photomultiplier tube.

The experimental system is shown in Figure 3.4. A plano-concave lens is used to expand a 7W continuous-wave laser beam (Verdi G7, $\lambda = 532$nm, Coherent Inc.), which illuminates a digital micromirror device (DMD, DLP3000, Texas Instruments) placed at the conjugate plane of the proximal end of the multicore fiber. The DMD has a maximum refresh rate of 4-kHz, and the laser is incident at 24° as the blaze condition is twice the tilt angle of the DMD mirrors. It should be noted that this CW laser drifts in wavelength within its linewidth, which impacts the long-term stability of the speckle patterns [48], [49]. Thus, for the best performance, we collect sets of 200 measurements within the drift-free period, and a single-frequency laser is preferable for future work. A white light LED and a condenser lens also illuminate the

proximal end of the multicore fiber with 1600 cores (FIGH-016-160S, Fujikura) with a 3-μm core diameter and 3.3-μm pitch. The CW laser and white light LED are coupled into the multicore fiber using a 20× finite conjugate objective lens, and camera **A** is used to image the fiber's proximal end. The rough surface of the ground glass diffuser (DG05-1500, Thorlabs) is placed 2-mm from the distal end of the multicore fiber, and the sample plane is another 2mm from this surface. The illumination diameters on the diffuser and on the sample plane are approximately 265-μm and 471-μm. This was experimentally reduced to 220-μm by an iris to facilitate CS recovery with up to 1000 measurements. A 10× objective lens is used after the sample plane to calibrate the random speckle patterns and collect single-photodetector measurements. The numerical aperture of the 10× objective lens only affects the fluorescence collection efficiency and does not affect the SBP of the imaging system. Camera **B** is used to calibrate the speckle patterns, while a photomultiplier tube (H7422-40, Hammamatsu) is used to collect the total light from the object. A long-pass dichroic mirror (DMLP550, Thorlabs) and filter (FEL0550, Thorlabs) are used to separate the excitation and fluorescence emission.

3.3.1 Image Registration

To register the fiber core positions, we image the input plane of the multicore fiber. Using a local maxima pursuit algorithm, we locate the spatial positions of each core, as shown in Figure 3.5. Next, the white light illumination is turned off, and the CW laser and the DMD are used to generate random control points within the field-of-view of the multicore fiber. The

image of the control points and the DMD input images are used to generate a two-dimensional geometrical transform that maps the spatial locations of individual fiber cores at the fiber input to the DMD mirrors (Fig. 3.5). Subsequently, 1000 DMD input images are generated to illuminate each fiber core sequentially using the CW laser, and the corresponding speckle patterns at the sample plane are measured. After this calibration, an object is placed at the sample plane, and the fiber cores are again sequentially illuminated while the PMT collects the total light from the object. These measurements and the calibrated speckle patterns are used to reconstruct the object using the TV minimization algorithm.
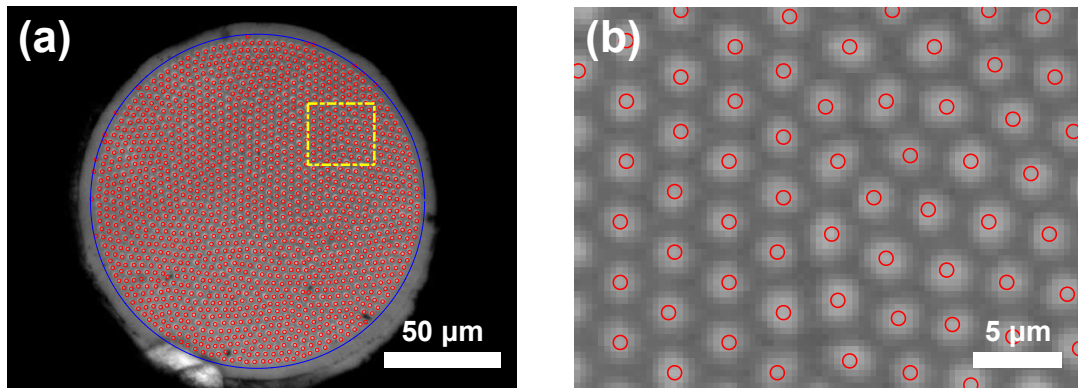
Figure 3.5: (a) White light illumination of the proximal end of the multicore fiber with individual cores spatially located using local maxima pursuit. **(b)** Magnified image of the yellow region in **(a)**.

3.3.2 Pattern Correlation

For the best imaging CS imaging performance, the sensing matrix must be uncorrelated within itself and with the sparsifying transform. To ensure this, the structured illumination patterns for two independent DMD scans without

any object in the field-of-view are acquired. The correlation between two random illumination patterns is calculated using the following:

$$\text{corr}(a, b) = \frac{\sum (a - \bar{a})(b - \bar{b})}{\sqrt{\sum (a - \bar{a})^2 \sum (b - \bar{b})^2}} \qquad (3.5)$$

where a and b are random illumination patterns from the first and second DMD scan, while $\bar{a}$ and $\bar{b}$ are the means of the corresponding images. The 2D correlation is calculated for all pairs of illumination patterns from the DMD scans to generate the correlation plot in Figure 3.6. The correlation between two independent random patterns should be close to 0, while like patterns should be near 1, demonstrating that the speckle patterns are uncorrelated but repeatable. As an example, Figure 3.6 **(a)** and **(b)** show two random speckle patterns generated by two adjacent fiber cores. Note that we chose a subset of 1000 fiber cores from the existing 1600 cores with the highest coupling efficiency, and the correlation did not impact which cores we chose.

3.4 Experimental Results

3.4.1 Fluorescence Imaging

Figure 3.7 shows the successful image recovery under different number of measurements. Figure 3.8 and 3.9 show image reconstructions of fluorescent particles (Nile Red, Spherotech) and resolution targets using 1000 measurements. While not optimized, reconstruction of a 100×100 pixels images using 1000 measurements took approximately 5-s. The left most column of Figure 3.8 shows widefield fluorescence images which are used as the ground truth.
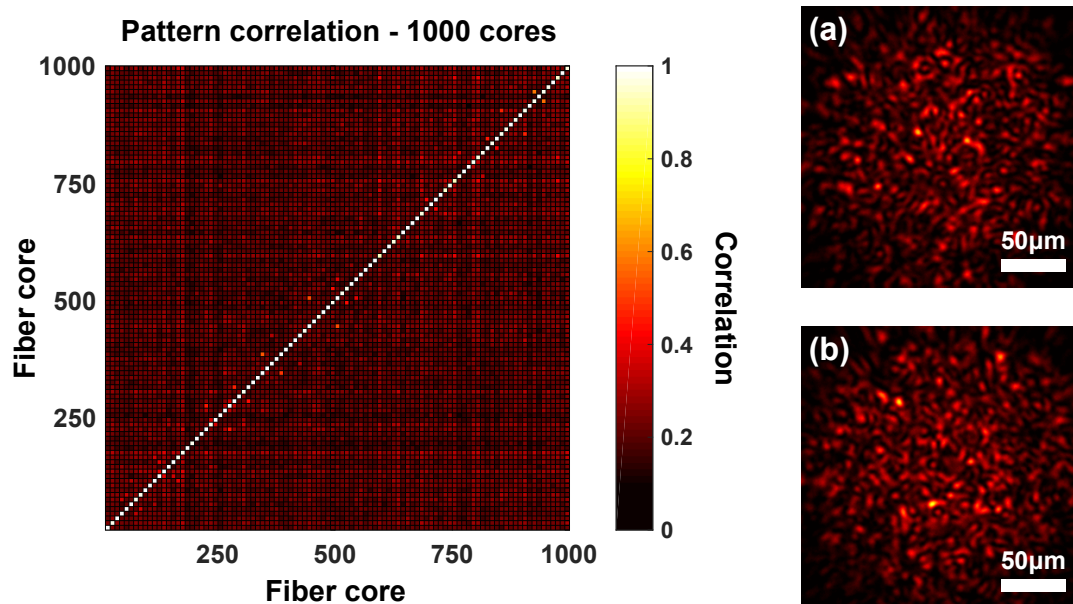
Figure 3.6: Correlation plot of the illumination patterns from 1000 individual fiber cores. **(a)** and **(b)** are speckle patterns generated from two adjacent fiber cores.
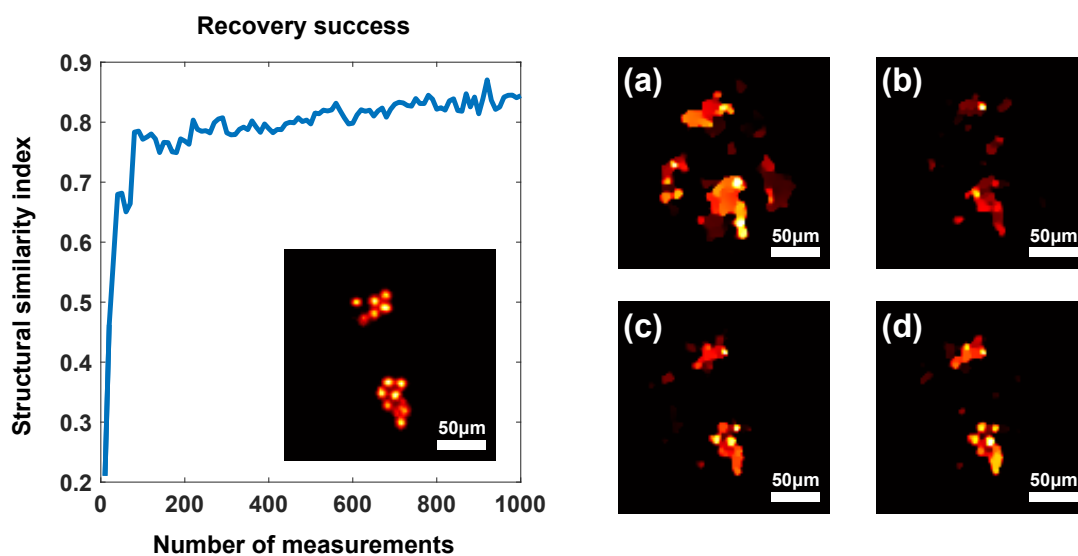
Figure 3.7: Plot of recovery success with respect to the number of measurements (fiber cores). The plot inset is the widefield fluorescence image of 10-μm fluorescent beads used as the ground truth. **(a)(b)(c)(d)** CS image reconstructions with 50, 100, 300, and 500 measurements. All images are 100×100 pixels and at 8-bit depth.

The field-of-view of the reconstructed images is 220-μm wide, which is larger than the multicore fiber's image circle diameter of 140-μm.
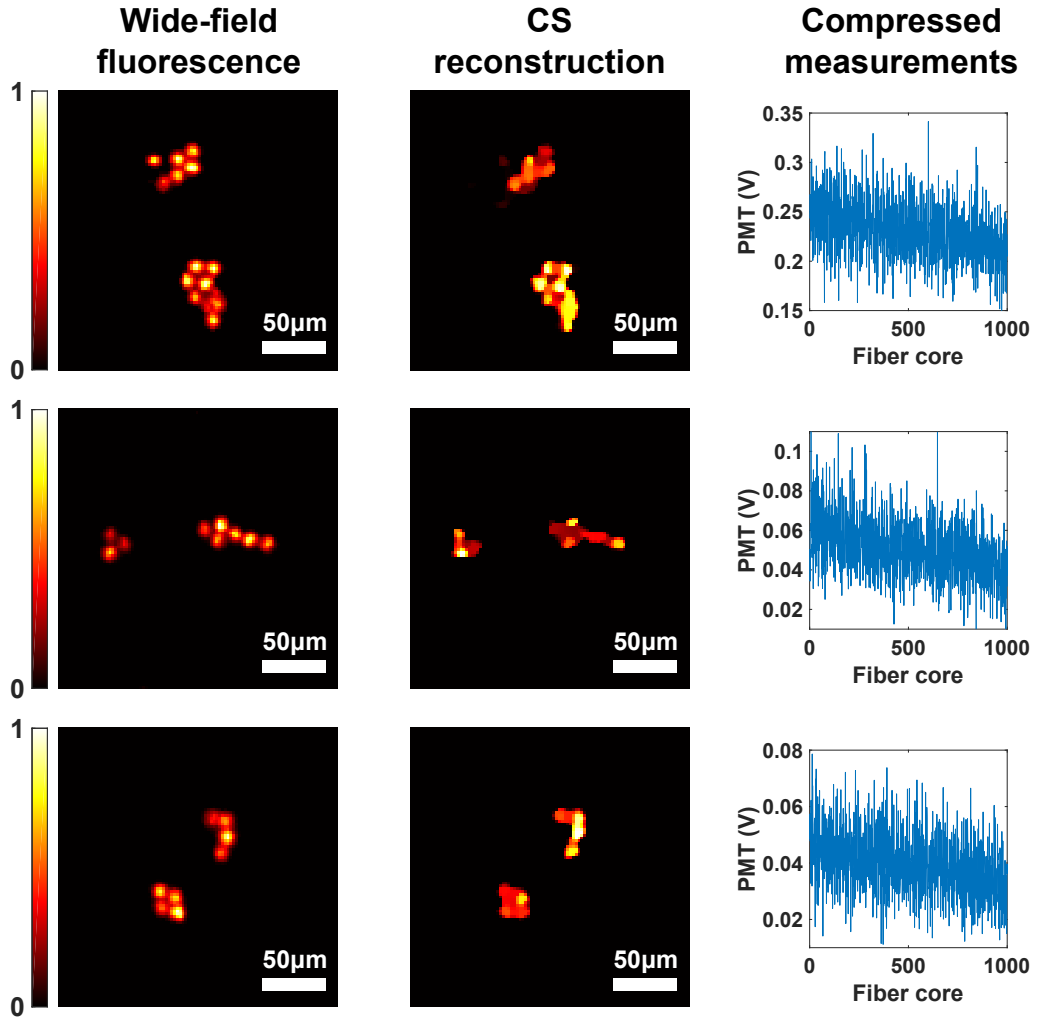
Figure 3.8: CS reconstruction of 10-μm fluorescent particles. Middle column shows reconstructions from 1000 measurements. Corresponding single-photodetector measurements used for image reconstruction are plotted in the right most column. All images are 100 $\times$ 100 pixels and at an 8-bit depth.
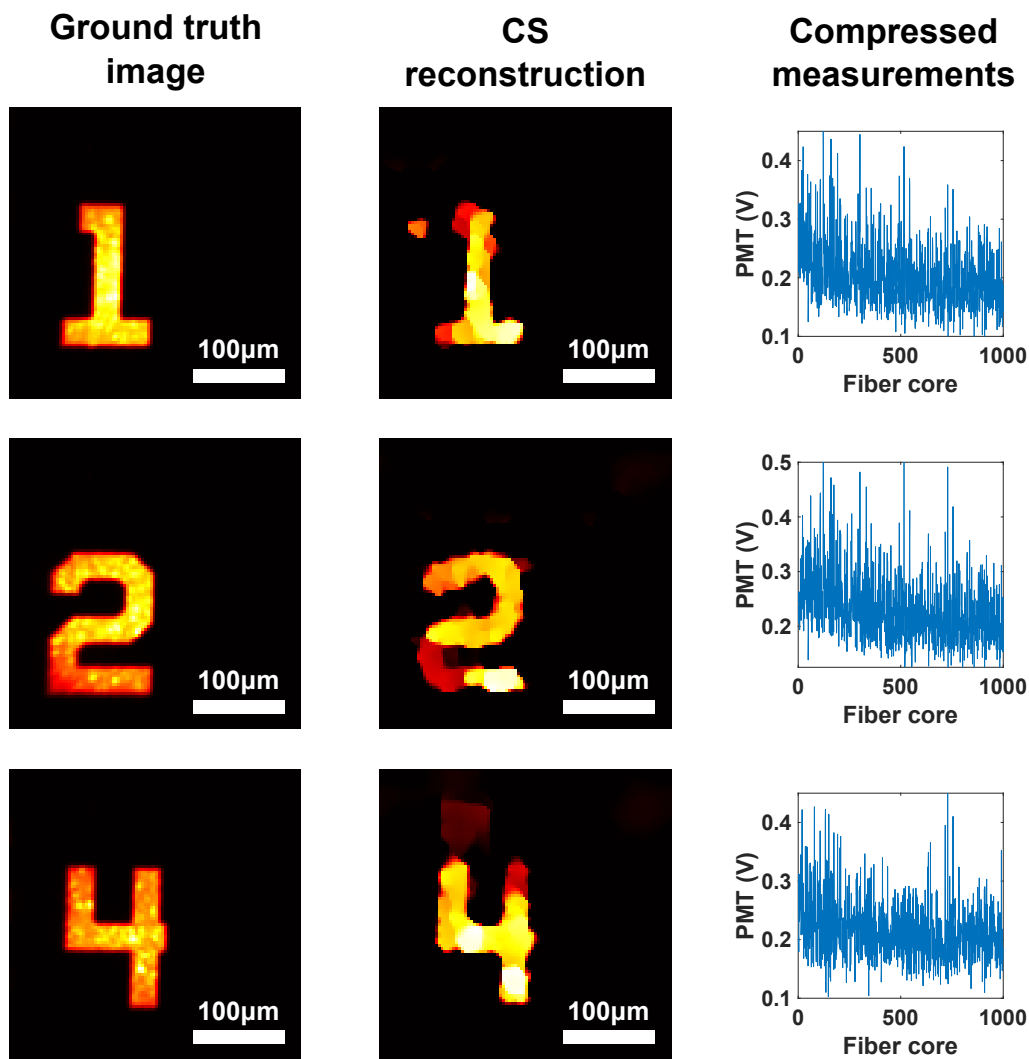
Figure 3.9: CS reconstruction of digits in a resolution target. Middle column shows reconstructions from 1000 measurements. Corresponding single-photodetector measurements used for image reconstruction are plotted in the right most column. All images are 100×100 pixels and at an 8-bit depth.
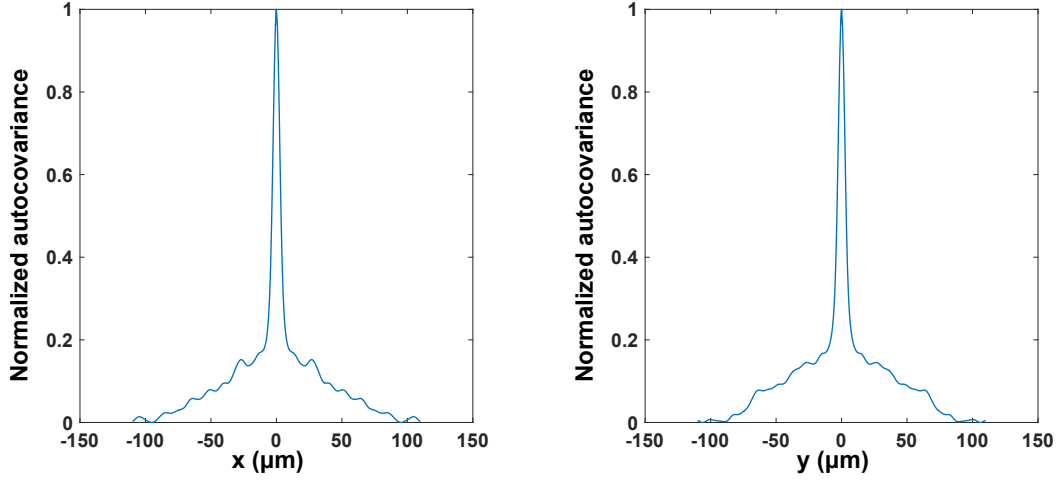
Figure 3.10: Autocovariances of 1000 structured illumination patterns used to determine the experimental spatial resolution.

3.4.2 Theoretical and Experimental Resolution

The spatial resolution of the proposed imaging system is determined by the speckle granule dimensions. Thus the normalized autocovariances of 1000 speckle patterns are calculated to determine the speckle size (Fig. 3.10) using the below equation:

$$c(x,y) = \frac{\mathcal{F}^{-1}\left\{|\mathcal{F}(I(x,y))|^2\right\} - \langle I(x,y)\rangle^2}{\langle I(x,y)^2\rangle - \langle I(x,y)\rangle^2} \tag{3.6}$$

where $c(x,y)$ is the autocovariance, $\mathcal{F}$ and $\mathcal{F}^{-1}$ are the Fourier and inverse Fourier transforms, $I(x,y)$ is the speckle intensity pattern, and $\langle \cdot \rangle$ is the mean operation.

With the assumption that speckle granules are Gaussian-shaped, the minimum feature size is calculated from the Gaussian full-width half-max of the horizontal and vertical cross-sections [51], which is approximately 4.8-μm.

Thus, the information capacity of the imaging system (SBP) is approximately $\frac{(220\mu m)^2}{(4.8\mu m)^2} \approx 2100$ resolvable features, and, for example, the image reconstruction in Figure 3.7 is generated with seven times fewer measurements than the SBP.

Notably, the theoretical far-field speckle feature size (Φ) can be approximated by $\Phi \approx \frac{\lambda d}{D}$ where λ = wavelength of light, d = distance from the diffuser to the sample plane, and D = illumination diameter on the diffuser [52]. The Gaussian beam radius from a fiber core is given by $w(z) = w_o \sqrt{1 + (\frac{z}{z_r})^2}$ where w_o = core radius, z = distance from the core, and $z_r = \frac{\pi w_o^2}{\lambda}$. Using the above approximations the theoretical minimum feature size is 4-μm, which matches well with our experimentally measured value.

3.4.3 Insensitivity to Fiber Bending
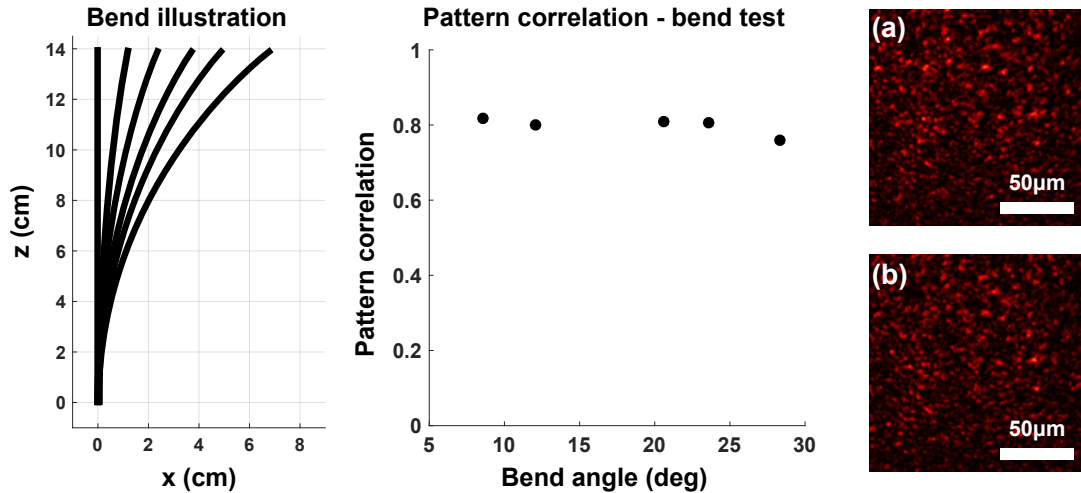
Figure 3.11: Correlation plot of the illumination patterns from a single core with different bending angles. Illustration of the bending is shown at the most left. **(a)(b)** are patterns without any bend and with 23.5º bend from its normal axis.

Figure 3.11 shows the correlations between speckle patterns generated

from the undisturbed fiber and under five different bending angles. It should be noted that the slight decorrelation of 0.8 are attributed to the crosstalk between cores and the excitation of higher-order modes within each core as the cores propagate a few modes at our laser wavelength. Using a multicore fiber with single-mode cores and a larger pitch ensures that the imaging system is completely bend-insensitive.

3.5   Discussion and Future Work

In conclusion, we have designed a compressive fluorescence imager using a multicore fiber with a scattering distal tip. By ensuring single-core illumination similar to a raster-scanning confocal microendoscope, the imaging system is insensitive to bending of the fiber. In addition, we reconstructed pixelation-free object images with an SBP of 2100 using between 300 and 1000 fiber cores in the multicore fiber. The future work will improve the efficiency and speed of the laser coupling into individual fiber cores utilizing two scanning galvo-mirrors. In addition, simultaneous light delivery and fluorescence collection using the multicore fiber is to be implemented.

Chapter 4

Single-Pixel Imaging Using Wavelength-Dependent Scattering

Previous chapter described a compressive imaging system that harnesses disorder to increase the information capacity of a multicore fiber. Similarly, this chapter presents an imaging system that pushes the limit of an imaging probe's invasiveness by using a single strand of optical fiber ($\varnothing < 125$-μm). A single-mode fiber with a multiply scattering tip and compressive sensing acquisition are employed to facilitate 2-dimensional imaging via structured illumination. A typical microendoscope using a single optical fiber for 2D imaging require a mechanical scanner or an actuator at the distal end to facilitate point-scanning of the scene. This lensless approach replaces such distal scanners with a multiply scattering tip. Unknown objects are illuminated with randomly structured, but deterministic, speckle patterns produced by a wavelength-swepth coherent light source propagating through a TiO_2-coated fiber tip. Experimentally, the coating thickness is optimized to produce speckle patterns that are highly sensitive to laser wavelength, yet repeatable. Images of the objects are reconstructed from the characterized wavelength dependence

of the speckle patterns and the wavelength dependence of the total light collected from the object using a single photodetector. The imaging device is mechanically scan-free and insensitive to bending of the fiber, making it suitable for ultra-thin microendoscopy.
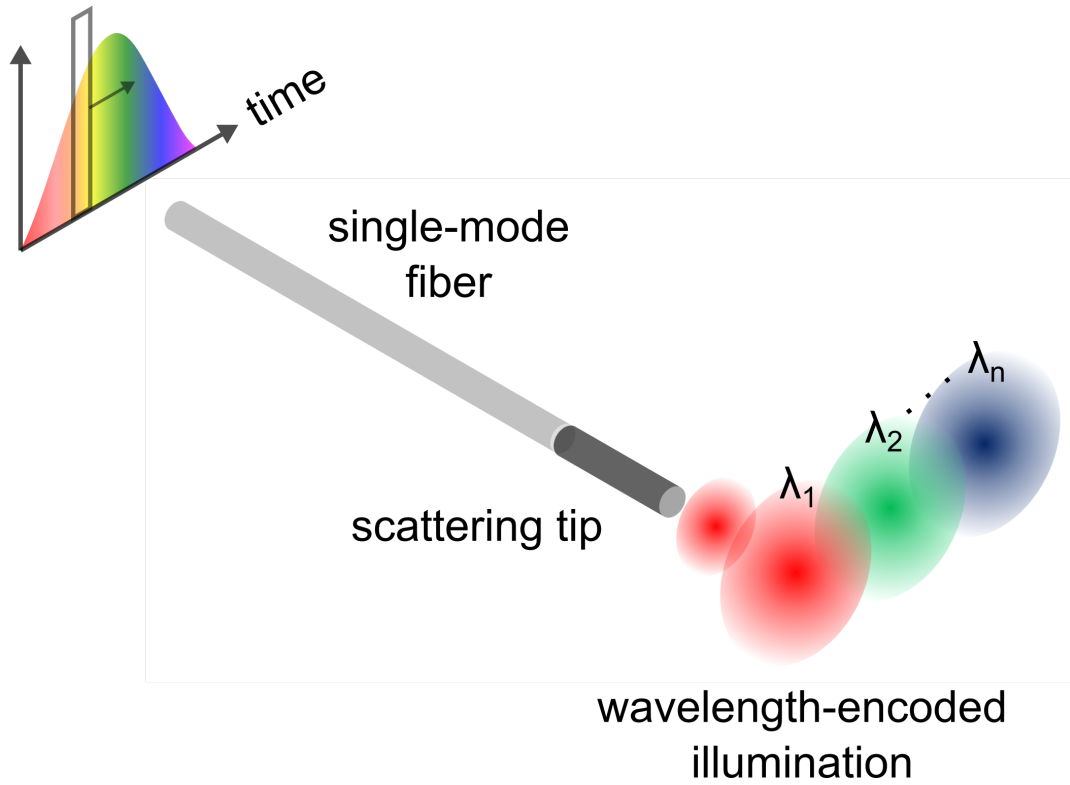
Figure 4.1: Conceptual illustration of the computational microendoscope using a single single-mode fiber with a distal scattering tip.

4.1 Mathematical Model

Let M and N represent the number of compressed measurements and the pixel dimensions of the object image ($N = n_1 \times n_2$). The observation vector

$y \in \Re^{M \times 1}$ can be expressed as follows:

$$y = Ax = \begin{bmatrix} A_1 x \\ A_2 x \\ \vdots \\ A_M x \end{bmatrix} \tag{4.1}$$

where $A_1, A_2, ..., A_M \in \Re^{1 \times N}$ are the vectorized wavelength-encoded illumination patterns for $\lambda_1, \lambda_2, ... \lambda_M$ and $x \in \Re^{N \times 1}$ are the vectorized object image to be recovered. The sensing matrix A consists of M random illumination patterns vertically concatenated where $A \in \Re^{M \times N}$. After building the sensing matrix A and the compressed measurements y from the optical hardware system, we can use an appropriate sparsity minimization algorithm to reconstruct the image of an unknown object x. For the following experimental results, we employed the patch-based iterative image reconstruction algorithm that was previously described in Chapter 2 (equation 2.5).

4.2   Experimental System

A block diagram of the experimental system is shown in Figure 4.2. The tunable continuous wave laser sweeps in wavelength from 1480 to 1569.9-nm in 0.1-nm increments to generate 1000 unique illumination patterns at the output of the 1.5-mm TiO$_2$-coated fiber tip. We experimentally determine that the TiO$_2$ coating as approximately 20% transmission of optical power. The light passes through a 20$\times$ objective lens to magnify the random illumination patterns at the object plane. The object plane is located one tube length away from the finite conjugate objective. A second focusing lens relays the

illumination patterns onto the infra-red camera for calibration. An iris is employed to define the field-of-view and ensure that the infra-red camera and the single photodetector share the same field-of-view after the beam sampler. Lastly, a 20× objective lens is used as a focusing lens to focus the light into the single photodetector. A neutral density filter is used to attenuate the light incident on the IR camera. The camera, photodetector, and tunable laser are controlled by a computer to automate the data acquisition.
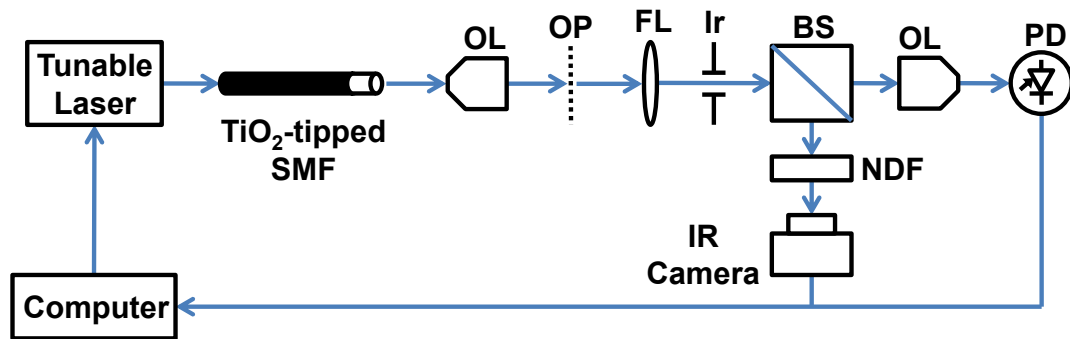
Figure 4.2: Experimental setup of the compressive imaging device. TiO_2-tipped SMF = single-mode fiber coated with 1.5-mm of TiO_2. OL = 20× objective lens, OP = object plane, FL = focusing lens, Ir = iris, BS = beam sampler, PD = photodetector, NDF = neutral density filter.

Two wavelength sweeps are performed to characterize the illumination patterns and then compressively acquire an image. The first sweep is performed for calibration of the imaging system, where random illumination patterns generated by the TiO_2-coated single-mode fiber are captured using the IR camera. At this stage, no object is placed at the object plane. The second sweep acquires the compressed measurements, where an object of interest (resolution target) is placed at the object plane. The random illumination patterns are projected onto the object, and their inner products are collected by the single photodetector.
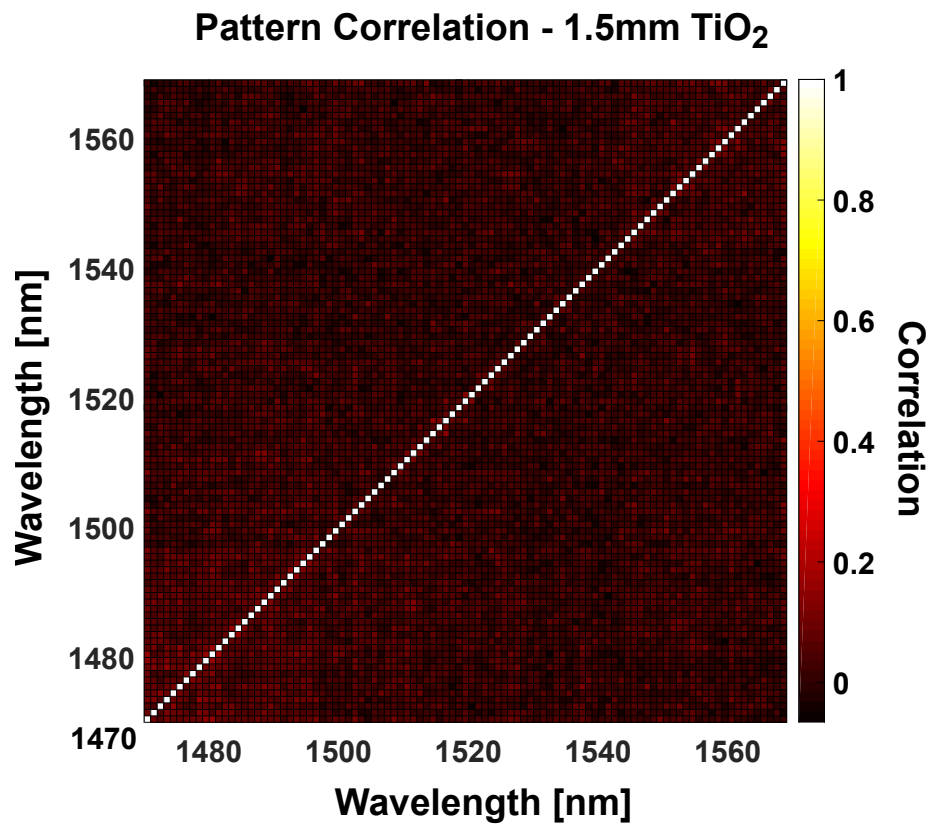
Figure 4.3: Pattern correlation plot of the wavelength-encoded illumination patterns generated by a single-mode fiber with TiO$_2$-tip of 1.5-mm thickness.

One major requirement of compressive imaging is that the sensing matrix must be highly uncorrelated within itself and with the sparsifying matrix to successfully reconstruct an object image. However, for this experimental system, there is an inherent trade-off between the randomness and repeatability of pattern generation, depending on the thickness of the scattering medium. Increasing the thickness of TiO_2 makes the illumination patterns more wavelength sensitive, ensuring that patterns from different wavelengths are maximally uncorrelated. However, if the illumination patterns are too wavelength sensitive, reliable calibration becomes difficult due to the limits on repeatability in the wavelength-stepped CW laser. Conversely, shortening the thickness of TiO_2 allows for repeatable randomness of each illumination pattern, which reduces the total number of informative measurements possible given a limited bandwidth of the CW laser. To optimize the pattern randomness and repeatability, the TiO_2 coating thickness is varied and the resulting illumination patterns for two independent wavelength sweeps are measured without any object placed in the object plane. The correlation between two random illumination patterns is calculated using

$$\mathrm{corr}(a,b) = \frac{\sum (a - \bar{a})(b - \bar{b})}{\sqrt{\sum (a - \bar{a})^2 \sum (b - \bar{b})^2}} \tag{4.2}$$

where a and b are random illumination patterns from the first and second sweep, while $\bar{a}$ and $\bar{b}$ are the means of the corresponding images. For a given thickness, a correlation is is calculated for all pairs of illumination patterns in the wavelength sweep to generate the correlation plot in, for example, Figure 4.3. The correlation among all of the wavelength-dependent patterns for these

two sweeps is shown in Figure 4.3 for a TiO$_2$ thickness of 1.5-mm. Note that the correlation between two independent patterns should be as close to 0 (the correlation of a pattern with itself will be 1), demonstrating that this thickness strikes an appropriate balance between randomness and repeatability. As an example, Figure 4.4 shows two random illumination patterns at different wavelengths and their corresponding projections onto an object of interest.
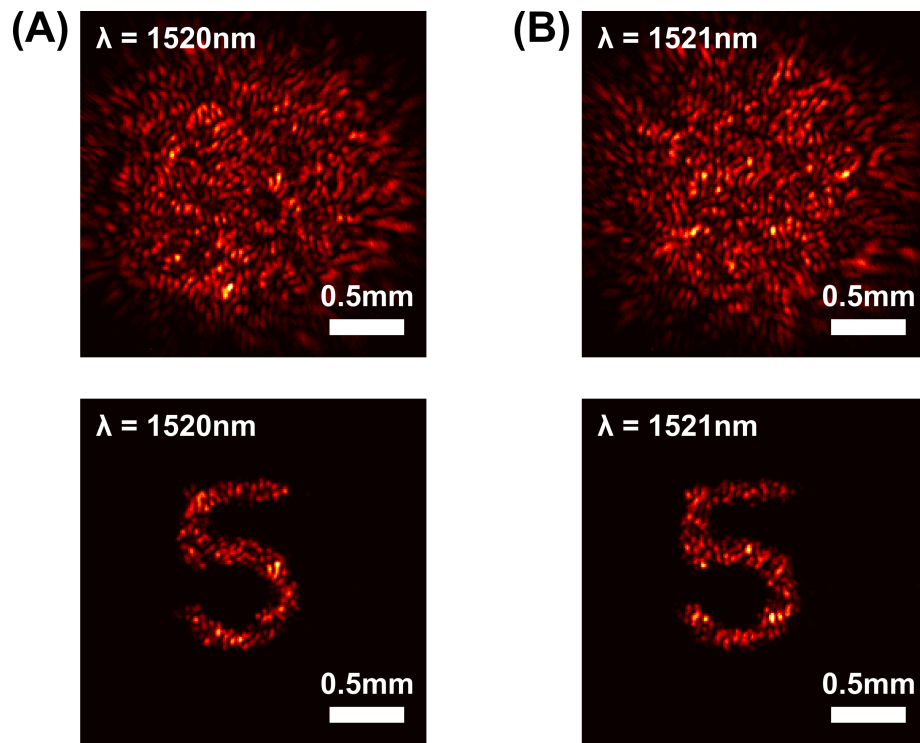
Figure 4.4: (a)(b) Random illumination patterns and their corresponding projections onto an object of interest at $\lambda = 1500$-nm and $\lambda = 1501$-nm.

4.3 Experimental Results

Figure 4.5 shows successful reconstruction of 64 $\times$ 64 pixel images from 1000 different wavelength measurements in a single sweep, which corresponds to

76

24% compression or $4\times$ sub-Nyquist rate. The left-most column and middle column, respectively, consist of actual images of the object taken with the IR camera and reconstructed images using the compressive measurements acquired with the single photodetector. The right most column shows the raw photodetector readings for the compressed measurements used in the sparsity minimization algorithm.

Although we assume sparsity in the DCT basis to recover binary images in this experimental system, the demonstrated imaging device is suitable for imaging generalized objects in, for example, an endoscopy or camera applications. The strength of pseudorandom sampling in CS imaging is that one can recover an object image, as long as it can be sparsely represented in some known basis. Real signals including images are known to be highly compressible as demonstrated in previous chapters. In other words, countless types of objects can be accurately imaged using the exact same set of physical measurements simply by employing a different sparsifying basis in the reconstruction algorithm.

Additionally, objects of interest embedded in a scattering volume can generate unwanted changes to the speckle pattern that can degrade the imaging performance of this system. This perturbation can be modeled for the reconstruction as additional noise n, varying by wavelength, added to the measurement patterns: $A' = A + n$. CS theory states that signal reconstruction will be successful provided the observations contaminated by noise, i.e., $y = A'x = Ax + w$, are bounded by a known amount $||w||_2 \leq \sigma$ [13]–[16]. In other words, one can successfully reconstruct object images provided the
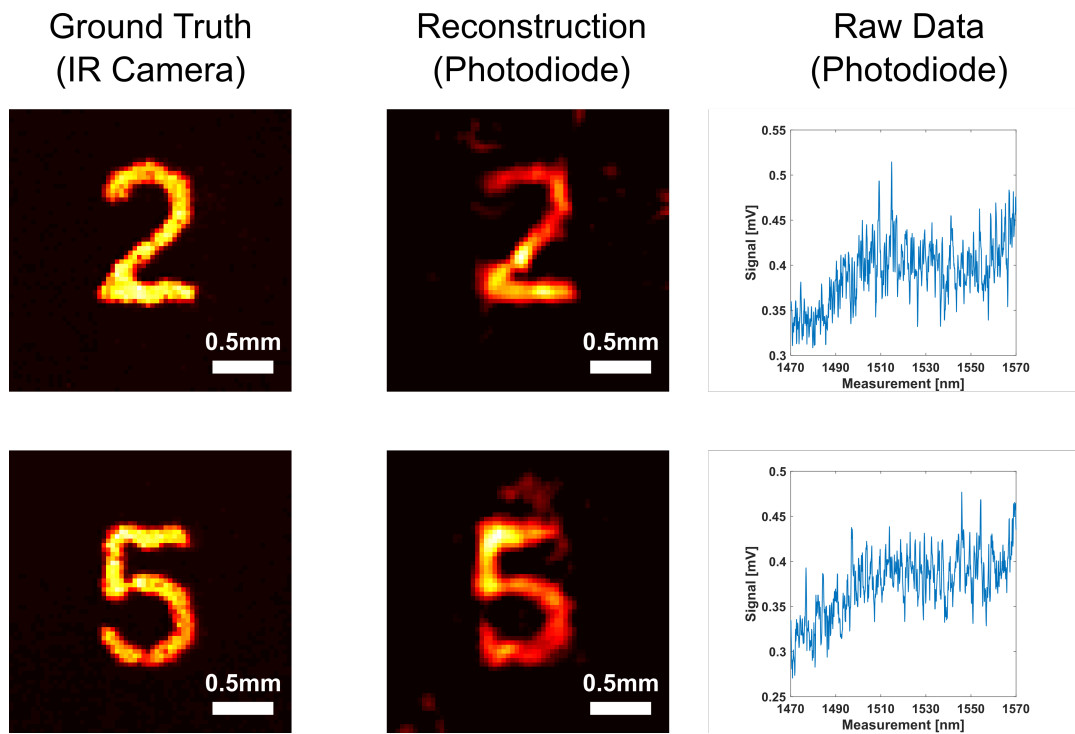
Figure 4.5: Reconstruction of digits from a a resolution target. Actual images of the objects taken with an IR camera are shown in the left-most column. Reconstruction results are shown in the middle column. Raw photodetector measurements used to reconstruct the images are plotted in the right-most column. Scale bar = 0.5-mm.

perturbations are small, while significant changes to the calibrated speckle patterns can degrade the image reconstruction.

4.4 Discussion and Future Work

In summary, we have designed a single-pixel compressive imager using a single-mode fiber coated with a wavelength-sensitive scattering medium. The proposed imaging technique is mechanically scan-free and insensitive to bending of the fiber, an advantage for microendoscopy applications, as well as wavelength-encoded high-throughput imaging [53]–[55]. In addition, an infra-red camera based on this approach can be very cost-efficient since it no longer requires a costly InGaAs image sensor commonly used for the near-IR spectrum. Toward endoscopy, one future approach is to use a dual-core fiber, where a small single-mode core is used for illumination and the light from the scene is collected back through the fiber using a much larger multimode core. In a fluorescence imaging application, the scattering medium thickness becomes more crucial since the number of wavelength-encoded measurements are limited by the fluorescence emission bandwidth of the fluorescent object. Thus, finding the thickness that simultaneously satisfies the randomness and the repeatability of the illmination patterns within the given fluorescence bandwidth is paramount. Additionally, beyond CS, multiply scattering media hold great potential as a superlens to exceed the diffraction limit of a conventional lens [43]–[47]. While the numerical aperture of a conventional lens is limited by its most oblique angle and, thus, its physical dimensions, scattering media allow for the collection of a wider range of

spatial frequencies of incoming light due to the multiple scattering process and thus higher space-bandwidth product. These additional benefits can also be leveraged in future realizations of this approach.

Chapter 5

Conclusion

This thesis has presented several lensless computational microendoscopes that simultaneously achieve miniaturization and high information content. Something as simple as a random amplitude mask at the distal end of a multi-core fiber enables recovery of a 3-dimensional volumetric scene from a single camera snapshot without any actuated parts. In addition, cheap and readily available scatters such as white paint can be used for minimally-invasive imaging with high-resolution and wide field-of-view. The presented ultra-thin microendoscopes show great potential for applications that demand extremely small and agile probes such as real-time imaging of neural activity in freely moving animals. Beyond microendoscopy, computational imaging techniques can be leveraged in imaging architectures that have strict limitations to the amount of acquired information. For example, a high-speed camera limited in the number of pixels for a given time, or a 3-dimensional fluorescence microscope limited in its imaging speed due to mechanical scanning bring to mind. Overall, the convergence of signal processing, optics with electronics, and sophisticated computational algorithms paves the way to next generation

imaging hardware.

Bibliography

[1] N. G. Horton, K. Wang, D. Kobat, C. G. Clark, F. W. Wise, C. B. Schaffer, and C. Xu, "In vivo three-photon microscopy of subcortical structures within an intact mouse brain," *Nature photonics*, vol. 7, no. 3, 2013.

[2] R. Prevedel, Y.-G. Yoon, M. Hoffmann, N. Pak, G. Wetzstein, S. Kato, T. Schrödel, R. Raskar, M. Zimmer, E. S. Boyden, *et al.*, "Simultaneous whole-animal 3d imaging of neuronal activity using light-field microscopy," *Nature methods*, vol. 11, no. 7, 2014.

[3] M. B. Bouchard, V. Voleti, C. S. Mendes, C. Lacefield, W. B. Grueber, R. S. Mann, R. M. Bruno, and E. M. Hillman, "Swept confocally-aligned planar excitation (scape) microscopy for high-speed volumetric imaging of behaving organisms," *Nature photonics*, vol. 9, no. 2, 2015.

[4] W. Yang, J.-e. K. Miller, L. Carrillo-Reid, E. Pnevmatikakis, L. Paninski, R. Yuste, and D. S. Peterka, "Simultaneous multi-plane imaging of neural circuits," *Neuron*, vol. 89, no. 2, 2016.

[5] K. K. Ghosh, L. D. Burns, E. D. Cocker, A. Nimmerjahn, Y. Ziv, A. El Gamal, and M. J. Schnitzer, "Miniaturized integration of a fluorescence microscope," *Nature methods*, vol. 8, no. 10, 2011.

[6] D. B. Aharoni and T. Hoogland, "Circuit investigations with open-source miniaturized microscopes: Past, present and future," *Frontiers in cellular neuroscience*, vol. 13, 2019.

[7] W. Zong, R. Wu, M. Li, Y. Hu, Y. Li, J. Li, H. Rong, H. Wu, Y. Xu, Y. Lu, *et al.*, "Fast high-resolution miniature two-photon microscopy for brain imaging in freely behaving mice," *Nature methods*, vol. 14, no. 7, 2017.

[8] Y. Ziv and K. K. Ghosh, "Miniature microscopes for large-scale imaging of neuronal activity in freely behaving rodents," *Current opinion in neurobiology*, vol. 32, 2015.

[9] A. A. Sharp, A. M. Ortega, D. Restrepo, D. Curran-Everett, and K. Gall, "In vivo penetration mechanics and mechanical properties of mouse brain tissue at micrometer scales," *IEEE Transactions on Biomedical Engineering*, vol. 56, no. 1, 2008.

[10] T. D. Kozai, A. S. Jaquins-Gerstl, A. L. Vazquez, A. C. Michael, and X. T. Cui, "Brain tissue responses to neural implants impact signal sensitivity and intervention strategies," *ACS chemical neuroscience*, vol. 6, no. 1, 2015.

[11] M. Young, "Pinhole optics," *Applied Optics*, vol. 10, no. 12, 1971.

[12] A. W. Lohmann, R. G. Dorsch, D. Mendlovic, Z. Zalevsky, and C. Ferreira, "Space–bandwidth product of optical signals and systems," *JOSA A*, vol. 13, no. 3, 1996.

[13] S. Mallat, *A wavelet tour of signal processing*. Elsevier, 1999.

[14] D. Taubman and M. Marcellin, *JPEG2000 image compression fundamentals, standards and practice: image compression fundamentals, standards and practice.* Springer Science & Business Media, 2012, vol. 642.

[15] E. J. Candès and M. B. Wakin, "An introduction to compressive sampling [a sensing/sampling paradigm that goes against the common knowledge in data acquisition]," *IEEE signal processing magazine*, vol. 25, no. 2, 2008.

[16] E. J. Candes, J. K. Romberg, and T. Tao, *Stable signal recovery from incomplete and inaccurate measurements*, 2006.

[17] M. F. Duarte, M. A. Davenport, D. Takhar, J. N. Laska, T. Sun, K. F. Kelly, and R. G. Baraniuk, "Single-pixel imaging via compressive sampling," *IEEE signal processing magazine*, vol. 25, no. 2, 2008.

[18] V. Studer, J. Bobin, M. Chahid, H. S. Mousavi, E. Candes, and M. Dahan, "Compressive fluorescence microscopy for biological and hyperspectral imaging," *Proceedings of the National Academy of Sciences*, vol. 109, no. 26, 2012.

[19] B. Lochocki, A. Gambıén, S. Manzanera, E. Irles, E. Tajahuerce, J. Lancis, and P. Artal, "Single pixel camera ophthalmoscope," *Optica*, vol. 3, no. 10, 2016.

[20] D. B. Phillips, M.-J. Sun, J. M. Taylor, M. P. Edgar, S. M. Barnett, G. M. Gibson, and M. J. Padgett, "Adaptive foveated single-pixel imaging with dynamic supersampling," *Science advances*, vol. 3, no. 4, 2017.

[21] M. S. Asif, A. Ayremlou, A. Sankaranarayanan, A. Veeraraghavan, and R. G. Baraniuk, "Flatcam: Thin, lensless cameras using coded aperture and computation," *IEEE Transactions on Computational Imaging*, vol. 3, no. 3, 2016.

[22] J. K. Adams, V. Boominathan, B. W. Avants, D. G. Vercosa, F. Ye, R. G. Baraniuk, J. T. Robinson, and A. Veeraraghavan, "Single-frame 3d fluorescence microscopy with ultraminiature lensless flatscope," *Science advances*, vol. 3, no. 12, 2017.

[23] A. Veeraraghavan, R. Raskar, A. Agrawal, A. Mohan, and J. Tumblin, "Dappled photography: Mask enhanced cameras for heterodyned light fields and coded aperture refocusing," in *ACM transactions on graphics (TOG)*, ACM, vol. 26, 2007.

[24] K. Marwah, G. Wetzstein, Y. Bando, and R. Raskar, "Compressive light field photography using overcomplete dictionaries and optimized projections," *ACM Transactions on Graphics (TOG)*, vol. 32, no. 4, 2013.

[25] B. A. Flusberg, E. D. Cocker, W. Piyawattanametha, J. C. Jung, E. L. Cheung, and M. J. Schnitzer, "Fiber-optic fluorescence imaging," *Nature methods*, vol. 2, no. 12, 2005.

[26] J. M. Jabbour, M. A. Saldua, J. N. Bixler, and K. C. Maitland, "Confocal endomicroscopy: Instrumentation and medical applications," *Annals of biomedical engineering*, vol. 40, no. 2, 2012.

[27] P. M. Lane, S. Lam, A. McWilliams, J. C. Le Riche, M. Anderson, and C. E. MacAulay, "Confocal fluorescence microendoscopy of bronchial epithelium," *Journal of biomedical optics*, vol. 14, no. 2, 2009.

[28] W. Lee and S. Yun, "Adaptive aberration correction of grin lenses for confocal endomicroscopy," *Optics letters*, vol. 36, no. 23, 2011.

[29] R. D. genannt Daweke, M. Kelp, H. Lehr, O. Mönnich, and P. Osiak, "Electromagnetic direct linear drives for medical endoscopes," in *2014 International Conference on Optimization of Electrical and Electronic Equipment (OPTIM)*, IEEE, 2014.

[30] Y. Zou, W. Zhang, F. S. Chau, and G. Zhou, "Miniature adjustable-focus endoscope with a solid electrically tunable lens," *Optics express*, vol. 23, no. 16, 2015.

[31] A. Li, W. Liang, H. Guan, Y.-T. A. Gau, D. E. Bergles, and X. Li, "Focus scanning with feedback-control for fiber-optic nonlinear endomicroscopy," *Biomedical optics express*, vol. 8, no. 5, 2017.

[32] B. N. Ozbay, G. L. Futia, M. Ma, V. M. Bright, J. T. Gopinath, E. G. Hughes, D. Restrepo, and E. A. Gibson, "Three dimensional two-photon brain imaging in freely moving mice using a miniature fiber coupled microscope with active axial-scanning," *Scientific reports*, vol. 8, no. 1, 2018.

[33] S. Turtaev, I. T. Leite, T. Altwegg-Boussac, J. M. Pakan, N. L. Rochefort, and T. Čižmár, "High-fidelity multimode fibre-based endoscopy for deep brain in vivo imaging," *Light: Science & Applications*, vol. 7, no. 1, 2018.

[34] E. R. Andresen, S. Sivankutty, V. Tsvirkun, G. Bouwmans, and H. Rigneault, "Ultrathin endoscopes based on multicore fibers and adaptive optics:

A status review and perspectives," *Journal of biomedical optics*, vol. 21, no. 12, 2016.

[35] G. Kim, N. Nagarajan, E. Pastuzyn, K. Jenks, M. Capecchi, J. Shepherd, and R. Menon, "Deep-brain imaging via epi-fluorescence computational cannula microscopy," *Scientific reports*, vol. 7, 2017.

[36] A. Porat, E. R. Andresen, H. Rigneault, D. Oron, S. Gigan, and O. Katz, "Widefield lensless imaging through a fiber bundle via speckle correlations," *Optics express*, vol. 24, no. 15, 2016.

[37] R. Y. Gu, R. N. Mahalati, and J. M. Kahn, "Design of flexible multi-mode fiber endoscope," *Optics express*, vol. 23, no. 21, 2015.

[38] A. M. Caravaca-Aguirre, E. Niv, D. B. Conkey, and R. Piestun, "Real-time resilient focusing through a bending multimode fiber," *Optics express*, vol. 21, no. 10, 2013.

[39] S. Farahi, D. Ziegler, I. N. Papadopoulos, D. Psaltis, and C. Moser, "Dynamic bending compensation while focusing through a multimode fiber," *Optics express*, vol. 21, no. 19, 2013.

[40] N. Stasio, C. Moser, and D. Psaltis, "Calibration-free imaging through a multicore fiber using speckle scanning microscopy," *Optics letters*, vol. 41, no. 13, 2016.

[41] S. Sivankutty, V. Tsvirkun, G. Bouwmans, D. Kogan, D. Oron, E. R. Andresen, and H. Rigneault, "Extended field-of-view in a lensless endoscope using an aperiodic multicore fiber," *Optics letters*, vol. 41, no. 15, 2016.

[42] M. Hughes, T. P. Chang, and G.-Z. Yang, "Fiber bundle endocytoscopy," *Biomedical optics express*, vol. 4, no. 12, 2013.

[43] I. M. Vellekoop, A. Lagendijk, and A. Mosk, "Exploiting disorder for perfect focusing," *Nature photonics*, vol. 4, no. 5, 2010.

[44] O. Katz, P. Heidmann, M. Fink, and S. Gigan, "Non-invasive single-shot imaging through scattering layers and around corners via speckle correlations," *Nature photonics*, vol. 8, no. 10, 2014.

[45] J. Bertolotti, E. G. Van Putten, C. Blum, A. Lagendijk, W. L. Vos, and A. P. Mosk, "Non-invasive imaging through opaque scattering layers," *Nature*, vol. 491, no. 7423, 2012.

[46] J. Min, J. Jang, D. Keum, S.-W. Ryu, C. Choi, K.-H. Jeong, and J. C. Ye, "Fluorescent microscopy beyond diffraction limits using speckle illumination and joint support recovery," *Scientific reports*, vol. 3, 2013.

[47] Y. Choi, T. D. Yang, C. Fang-Yen, P. Kang, K. J. Lee, R. R. Dasari, M. S. Feld, and W. Choi, "Overcoming the diffraction limit using multiple light scattering in a highly disordered medium," *Physical review letters*, vol. 107, no. 2, 2011.

[48] J. Shin, B. T. Bosworth, and M. A. Foster, "Single-pixel imaging using compressed sensing and wavelength-dependent scattering," *Optics letters*, vol. 41, no. 5, 2016.

[49] J. Shin, B. Bosworth, and M. A. Foster, "Compressive fluorescence imaging using a multi-core fiber and spatially dependent scattering," *Optics letters*, vol. 42, no. 1, 2017.

[50] C. Li, W. Yin, H. Jiang, and Y. Zhang, "An efficient augmented lagrangian method with applications to total variation minimization," *Computational Optimization and Applications*, vol. 56, no. 3, 2013.

[51] Y. Piederrière, J. Cariou, Y. Guern, B. Le Jeune, G. Le Brun, and J. Lotrian, "Scattering through fluids: Speckle size measurement and monte carlo simulations close to and into the multiple scattering," *Optics Express*, vol. 12, no. 1, 2004.

[52] M. Giglio, M. Carpineti, A. Vailati, and D. Brogioli, "Near-field intensity correlations of scattered light," *Applied Optics*, vol. 40, no. 24, 2001.

[53] K. Goda, K. Tsia, and B. Jalali, "Serial time-encoded amplified imaging for real-time observation of fast dynamic phenomena," *Nature*, vol. 458, no. 7242, 2009.

[54] A. M. Weiner, "Ultrafast optical pulse shaping: A tutorial review," *Optics Communications*, vol. 284, no. 15, 2011.

[55] K. Goda and B. Jalali, "Dispersive fourier transformation for fast continuous single-shot measurements," *Nature Photonics*, vol. 7, no. 2, 2013.

Vita

Jaewook Shin was born in September 4, 1991 in Seoul, Republic of Korea (South). He finished elementary education in Korea and moved to Toronto, Canada for high school. He completed his B.S. (2013) in Electrical Engineering with general and departmental honors at Johns Hopkins University, and pursues a Ph.D. at the same institution. His work focuses on optical imaging, sensing, and computational imaging, and can be found in Science Advances, Optics Letters, and various conference proceedings including *Conference on Lasers and Electro-Optics* and *SPIE Photonics West*. He has served as a reviewer for Optics Express, Applied Optics, Optics Letters, and Biomedical Optics Express.